VIBRATION BASED PLANETARY GEAR ANALYSIS AND DAMAGE DETECTION

A Thesis

presented to

the Faculty of California Polytechnic State University,

San Luis Obispo

In Partial Fulfillment

of the Requirements for the Degree

Master of Science in Mechanical Engineering

by

René Peter Dominic Sawatzky

September 2014

COMMITTEE MEMBERSHIP

TITLE:	Vibration Based Planetary Gear Analysis and Damage Detection
AUTHOR:	René Peter Dominic Sawatzky
DATE SUBMITTED:	September 2014
COMMITTEE CHAIR:	Xi Wu, PhD Associate Professor of Mechanical Engineering
COMMITTEE MEMBER:	James Meagher, PhD Professor of Mechanical Engineering
COMMITTEE MEMBER:	Frank Pöhler, PhD Professor of Mechanical Engineering

ABSTRACT

Vibration Based Planetary Gear Analysis and Damage Detection

René Peter Dominic Sawatzky

With this thesis the research at the engineering department is continued, based on previous thesis projects. These projects were considering the possibility of simulation gears with rigid bodies. After researches with different emphasizes on the rigid body simulation, the gained knowledge showed limitations of the rigid body model. Gear failures are very diverse and the actual simulation technique could not represent all necessary failure modes that can occur. That led to this thesis as a research project to find a way to detect and analyze the failure modes that cannot be considered with the current rigid body approach. With the flexible body theory and simulation tools (MSC:Adams) this gap of gear failure detection simulation can be closed. The objective is, making it possible to simulate all failure modes of a gear that can occur. Additionally the previous project on this topic were using gears of small laboratory conditions. An industry sector has been picked to work on a practical application. This application is a wind turbine gearbox. These gearboxes have common run-time errors which influences the profitability of the power generation. To model this system a gear design guide for wind turbine gearboxes is elaborated.

Keywords: Planetary gear design, vibration based damage detection, wind turbine, gear failure

ACKNOWLEDGMENTS

This thesis is the completion of the dual degree program, an agreement on graduate student exchange program to a double master's degree in engineering, between the Karlsruhe University of Applied Sciences (Hochschule Karlsruhe – Technik und Wirtschaft) in Germany and the California Polytechnic State University in San Luis Obiso, USA. The agreement was signed in Mai 2010 starting in September of the same year. I joined the program with the beginning of my masters in Karlsruhe in September 2011 and moving to San Luis Obispo in September 2012. The elaboration of the thesis was written at the engineering department of the California Polytechnic State University. Therefore is the thesis format according to the American standards and principles.

This exchange program has a major positive impact of my life. Hence, I want to thank Prof. Dr. Wolf-Immo Jutzler for introducing and helping me to join this program. I also want to thank Prof. Xi (Julia) Wu for support, advice and help during the project.
Next to the academic excellence of both universities, the experiences I have made during this time are influencing my life in a way that I did not expect. I am thankful for the dear friends I could find and the colleagues I was allowed to work with. The biggest gift, my wife and I brought home from the USA, is our lovely daughter Lea Grace who was born on 28 December 2013 in San Luis Obispo.

TABLE OF CONTENTS

Page

List of Tables x

List of Figures xi

1 Introduction 1

1.1 Problem Definition 1

1.2 Literature Review 2

1.3 Current Status of the Problem Research at Cal Poly and objectives of the Thesis 4

2 Wind Turbine Energy Conversion 6

2.1 Introduction to Wind Turbines 6

2.2 Theory for maximum Energy generation for wind turbines 8

2.3 Practical Power generation in wind turbines (Nordex N90) 12

3 Gear Failure 15

3.1 Gear Failure Modes 15

3.1.1 Tooth breakage 16

3.1.2 Tooth flank failure 18

3.2 Frequency of Failure Modes of Wind Turbine Gears 20

3.3 Forces at the Tooth of the Gear 20

3.4 Factors of Load Influence 22

3.5 Tooth Root Load Capacity 23

4 Gear Design for Wind Turbines 24

4.1 Design of Planetary Gears 24

4.2 Parts and Structure of a Standard Planetary Gear 25

4.3 Gear Ratio & Number of Teeth for Ring and Sun Gear 25
4.4 Pitch diameters & Number of Teeth for Planets 27
4.5 Design Properties for Planetary Gears 28
4.5.1 Necessary Design Properties 28
4.5.2 Preferred Design Properties 29
4.6 Simplified Guidance for Planetary Gear Boxes of Wind Turbines 29
4.7 Verification 30
4.7.1 Tooth Strength Verification 31
4.7.2 Load Capacity of the Tooth Flank Verification 33
4.8 Backlash of Gears 35
4.9 Power & Torque 37
4.10 Relative Speeds 38
5 Multi Body Dynamics Simulation in MSC.Adams 39
5.1 Simulation Process 39
5.1.1 CAD – AutoCAD Inventor 40
5.1.2 FEM – Abaqus 40
5.1.2.1 Node definition 41
5.1.2.2 Element, Element Property and Material Definition 42
5.1.2.3 Modal Analysis 43
5.1.2.4 Substructure Generation 43
5.1.3 MNF – Abaqus Interface for ADAMS 44
5.1.4 MBD – MSC.Adams 44
5.2 Theory of Flexible Bodies 46

5.2.1 Modal analysis 46
5.2.2 Modal Superposition 48
5.2.3 Modal flexibility in Adams 48
5.2.4 Verification of Applied Flexible Body Theory 53
5.3 Simulation Step Size 56
5.4 Stiffness Value and Contact Forces 58
5.4.1 Theory to Approach Solutions of Contact Forces and Stiffness 58
5.4.2 Penetration Depth 61
5.4.3 Damping 61
5.4.4 Force exponent 61
6 Analysis of Multi Body Dynamics Simulation of Wind Turbines 62
6.1 The Simulated System 62
6.1.1 Overview 62
6.1.2 The Gearbox 63
6.1.3 Input Force 65
6.1.4 Relative speeds 65
6.1.5 The Generator 66
6.2 Damaged tooth, cracked sun gear tooth 66
6.3 Tooth root damage detection 67
6.4 Gear Mesh Frequency (GMF) 69
6.5 Fast Fourier Transform (FFT) 70
6.6 Vibration Results Analysis 72
6.7 Operating Numbers 74

7 Recap and Perspective 79

References 80

Appendices

Appendix A: Gear Design Guide in Microsoft Excel 83

Appendix B: Simulation Parameters 88

LIST OF TABLES

Page

Table 2-1: Nordex N90/2300 spec sheet [3] 13

Table 4-1: Reference of given values (blue filled boxes) 32

Table 4-2: Reference of given values (blue filled boxes) 34

Table 5-1: Material properties of the simulated gear 40

Table 5-2: Deflection calculation comparison of different calculation methods 54

Table 5-3: Comparison of the deflection of a tooth for different calculation methods 55

Table 6-1: Parameter of the gearbox for N90/2300 [3, p. 7] 63

Table 6-2: Parameter of the 1st and 2nd stage 64

Table 6-3: Relative speeds of 1st stage 66

Table 6-4: Standard Deviation of the FFT markers and
Operating Numbers for a Perfect Gear 76

Table 6-5: Standard Deviation of the FFT markers and
Operating Numbers for a Middle Crack 76

Table 6-6: Standard Deviation of the FFT markers and
Operating Numbers for a Long Crack 77

Table 6-7: Standard Deviation of the FFT markers and
Operating Numbers for an Extra Long Crack 77

LIST OF FIGURES

Page

Figure 2-1: Darrieus wind turbines (Reference [18]) 6
Figure 2-2: Typical horizontal axis wind turbine (Reference [1]) 6
Figure 2-3: Typical megawatt wind turbine (Reference [1]) 7
Figure 2-4: Four groups of main parts of a wind turbine 8
Figure 2-5: Widening of the cross-section (Reference [2, p. 264]) 9
Figure 2-6: Power coefficient over ratio of wind speeds 11
Figure 2-7: Power coefficient curve of a Nordex n90/2300 wind turbine 12
Figure 2-8: Power and torque related to the wind speed 14
Figure 3-1: Breakage and fatigue of gear teeth 16
Figure 3-2: Typical tooth root breakage (Reference [23, p. 2]) 16
Figure 3-3: Typical tooth flank breakage (Reference [23, p. 2]) 16
Figure 3-4: Fatigue breakage (Reference [4, p. 3]) 17
Figure 3-5: Fatigue breakage (Reference [4, p. 5]) 18
Figure 3-6: Inclusion origin on tooth fragment (Reference [4, p. 10]) 18
Figure 3-7: Close-up of origin (Reference [4, p. 11]) 18
Figure 3-8: Overview of tooth flank failure 19
Figure 3-9: Wear (scuffing) (Reference [5, p. 13]) 19
Figure 3-10: Corrosive wear (fretting corrosion) (Reference [5, p. 17]) 19
Figure 3-11: Flank fatigue (Pitting) (Reference [4, p. 22+23]) 19
Figure 3-12: Flank fatigue (subcase fracture) (Reference [6]) 19
Figure 3-13: Deforamtion (Reference [6]) 20
Figure 3-14: Flaws (hardening cracks) (Reference [7, p. 13]) 20
Figure 3-15: Recorded gearbox incidents summary from the NREL database 20
Figure 3-16: Tooth forces for spur gear ($\beta = 0°$) 21
Figure 3-17: Tooth forces for spur gear ($\beta > 0°$) (Reference [9, p. 745]) 21

Figure 3-18: Tooth stress (Reference [9, p. 704]) 23
Figure 4-1: Simple planetary gear (Reference [15]) 25
Figure 4-2: Planetary gear 25
Figure 4-3: Ring gear notation 26
Figure 4-4: Summary of calculations from chapter 4.3 27
Figure 4-5: Summary of calculations from chapter 4.4 28
Figure 4-6: Simplified guidance for planetary gear boxes of wind turbines 30
Figure 4-7: Tooth strength verification guidance 31
Figure 4-8: Load capacity of the tooth flank verification guideance 33
Figure 4-9: Backlash at gear teeth (Reference [9, p. 734]) 36
Figure 4-10: Mesh load factor $K\gamma$ (Reference [10, p. 37]) 37
Figure 5-1: Simulation process for rigid bodies 39
Figure 5-2: Simulation process for flexible bodies 39
Figure 5-3: Command window of the Abaqus interface for ADAMS 44
Figure 5-4: User interface MSC.Adams 45
Figure 5-5: Mode of a flexible body in MSC.Adams 45
Figure 5-6: Deformed tooth during simulation 46
Figure 5-7: The position vector to a deformed point P' on a flexible body relative 49
Figure 5-8: Simple structural beam geometry 53
Figure 5-9: Simulated gear 56
Figure 5-10: Contact force of gear teeth with step size of 0.1 seconds 56
Figure 5-11: Contact force of gear teeth with step size of 0.05 seconds 57
Figure 5-12: Contact force of gear teeth with step size of 0.01 seconds 57
Figure 5-13: Contact force of gear teeth with step size of 0.05 and 0.01seconds 57
Figure 5-14: Contact force of gear teeth with step size of 0.001 seconds 58
Figure 5-15: Line contact at gear contact (Reference [9, p. 83]) 58
Figure 5-16: Extended approach of contact of cylindrical bodies (Reference [12, p. 130]) 59
Figure 5-17: Approximation of tooth radius 60

Figure 6-1: Nordex wind turbine (Reference [1]) 62
Figure 6-2: Inside nacelle of the Nordex wind turbine (Reference [1]) 63
Figure 6-3: Gears of 1st stage 65
Figure 6-4: Generated power and torque 65
Figure 6-5: Operational points of a wind turbine with two asynchronous generators 66
Figure 6-6: Tooth Root Cracks on the Sun Gear 67
Figure 6-7: Contact force of perfect gear vs. tooth root breakage, step size of 0.01 68
Figure 6-8: Contact force of perfect gear vs. tooth root breakage, step size of 0.01 68
Figure 6-9: Time until new tooth contact 69
Figure 6-10: Decomposing a function (Wikipedia) 70
Figure 6-11: Sine function 100N*sin(time) 70
Figure 6-12: FFT for a simple sine curve 71
Figure 6-13: Different components of a signal 71
Figure 6-14: FFT of a periodical tooth contact force 72
Figure 6-15: FFT of the contact force at the sun gear stage 1 72
Figure 6-16: Zoom of the noise of the perfect gear 73
Figure 6-17: Comparison of the Cracked and Perfect Gear 74
Figure 6-18: FFT of a cracked gear 1st stage 75
Figure 6-19: Increasing vibration noise with larger cracks 78

1 INTRODUCTION

In this chapter an **abstract** of the thesis will be presented. Furthermore, the **problem definition** is described in 1.1 respectively. Finally, in section 1.2 a short overview about the **current status of the problem research at Cal Poly and objectives of the thesis** is provided and how this thesis will build on the knowledge already gained. It also shows what the objectives are to improve the current status of development.

1.1 Problem Definition

Of the earth's wind power, an estimated 72 terawatt is commercially available. This is more than enough power to supply the global community with electric energy. The global power consumption can be estimated to about 19tW[1]. However, wind energy has limitations in supplying constant energy over time. Wind turbines are dependent on the weather and will therefore never be the only energy source. Additionally, high wind turbine towers are changing the shape of the landscape and are not preferred by a significant number of people. However, even with these limitations, wind power can play a major role as green energy resources. Offshore wind parks especially are able to supply an significant amount of energy. The actual development is clearly in favor of wind energy and with improvement in technology and reliability this development will keep on growing. Depending on the design of the systems, wind turbine can generate up to 5 MW of energy, supplying up to 1500 homes.

The industry of renewable energy through wind turbines is virtually exploding in growth. Due to recent catastrophic events like the Fukushima nuclear disaster in March 2011 and general belief in climate change due to human influences, this trend will keep on going. This industry enjoys a high government support. One of the most significant issues that raise complaints about the wind turbine system is, that the predicted/promised energy gain over the planned lifetime cannot be

---

[1] Reference [28]

For the Cal Poly Formatting Guidelines see reference [41]

realized. One of the main reasons for this is that the gearboxes which have a designated lifetime of 20 years are fail in a shorter period of time. Most wind turbines which were originally designed to run for 20 years require significant repairs or complete overhauls in a 5-7 year range. The major operating cost for wind turbines is the high cost of repairs. Gearboxes are one of the primary reasons for increasing the cost to generate energy from theses free renewable resources.

Most of the downtime of wind turbines is due to gearbox issues. The cost of a gearbox replacement for a 1.5mW turbine can run to more than $250,000. Including labor, crane rental and lost profits. The crane that is needed for this type of job is very rare. Because of this, the downtime for wind turbines can reach several weeks until the necessary equipment is available. Gearbox failures have been a problem from the beginning of the design of wind turbines. Design flaws account for most of the problems with gearboxes. Another problem is load estimates which are too optimistic. Researchers work together to establish standards for wind turbine gearbox design. However, the gear box failure rate is still high and expensive. The National Renewable Energy Laboratory's (NREL) Gearbox Reliability Collaborative (founded in 2007) is a cooperative of research professionals, manufacturers, owners, operators and consultants. Together they seek to identify shortcomings in the design, testing and operation of wind turbines that contribute to reduced gearbox reliability.

1.2 Literature Review

Discussions about modeling and dynamical analysis of gear systems have been done by Özgüven/Houser[2] and Parey/ Tandon[3]. The majority approach of the models in these papers include a limited number of degrees of freedom. However they do not consider tooth defects in

[2] Reference [32]

[3] Reference [33]

the parts. In a different publication from Parey/Tandon[4], they considered approaches that include defects.

Lin and Parker[5] analyzed the dynamical behavior of planetary gears due to a variation of the gear mesh stiffness. To build mathematical models of the dynamic behavior of gears, Professor Parker and his team completed significant research of planetary gears. Lin and Parker[6] derived a theoretical model to identify the natural frequencies and vibration modes for planetary gears. However, the majority of scientific papers about planetary gears do not include the effects of gear teeth damage.

Gear damages at the teeth making it extremely difficult for a theoretical approach. But gear damages such as cracks are a potential source of failure of the whole gearbox. Failure can occur due to fatigue, overload or manufacturing errors. Due to significant importance to detect gear failures, a lot of effort has been expended to improve and develop reliable ways for the detection. Hence, most of the approaches have fallen short of the required reliability. A robust approach that can determine the health of a gearbox could find a good reception across many industries and applications.

With MSC.Adams software it is possible to realistically simulate the dynamic behavior of gears. Kong and Meagher[7] simulated a contact of a gearbox without backlash. In a later publication Sommer and Meagher[8] illustrated the transient and steady state dynamic loading on teeth with backlash and geometric manufacturing errors. For different initial velocities and load conditions the vibration behavior and impact force distinctions has been shown. Further studies have been completed by Wu, Meagher and Sommer[9] for a practical differential planetary gear system. Therefore, errors at the tooth profile have been designed and compared with perfect gears. With

---

[4] Reference [33]

[5] Reference [35]

[6] Reference [36]

[7] Reference [37]

[8] Reference [38]

[9] Reference [39]

the multi body dynamic simulation software new problems occur. A lot of parameter have to be chosen to simulate the correct real world behavior of a system. In 2012 Giesbers[10] showed an overview about parameters of the simulation. Earlier, in 2006 Parey etc.[11] developed a six DOF model for a pair of spur gears on two shafts and calculated the Hertzian stiffness for the tooth surface contact. To simulate defects in gears, the authors implemented an empirical mode decomposition (EMD) method to realistically simulate different defects. A Hertzian tooth stiffness theoretical approach is also considered by Johnson[12] and has been applied with “HertzWIN” by Vink System Design & Analysis. At this approach, each tooth is, for simplification, assumed to be cylindrical bodies. Hence, the radius of the contact teeth has to be approximated and can be used for the theoretical Hertzian approach.

1.3 Current Status of the Problem Research at Cal Poly and objectives of the Thesis

Several different approaches are available to monitor gearbox conditions. Low tech monitoring such as visual inspection and the inspection of the filter elements are standard processes that will be performed during a maintenance inspection of the wind turbine. The drawback of this methods is that it does not provide live-monitoring. This means that a problem in the gearbox can just be detected when it is checked in person on site. Even then, a crack on the gear tooth may be not recognized by the maintenance technician.

Other live-monitoring methods are metal detectors. These units detect metal parts in the oil of the gear box. This method has a significant limitation in reliability, because the loose parts have to pass right in front of the metal detector. On the other hand, it is a good method to detect wear of the gear.

Live-monitoring through vibration analysis is also available. This is by far the most promising inspection method for gear boxes. If vibration can detect all different kinds of failure or wear of the

[10] Reference [1]

[11] Reference [34]

[12] Reference [12]

gears, it could be a sufficient inspection method. Additionally vibration can be monitored online via a gsm module allowing the damage to be detected at any time by the maintenance technician. Previous works at the Cal Poly Mechanical Engineering Department have confirmed the reliability of the vibration analysis for different kind of gear problems. Gears have been monitored and analyzed in the vibration lab. Furthermore, the lab experiments were done by conditions with chosen parameters, such as gear types, forces and speeds that would lead to good results. One point of this thesis is to apply the Multi Body Dynamic Simulation to an industry problem.

As a result of the previous lab analysis, the Multi Body Dynamic Simulation with MSC.Adams has been verified. All results of the practical lab approved the simulation. However, the simulation was based on rigid body simulation. This kind of simulation has a limitation which excludes certain types of gear damages for the analysis. A rigid body simulation can just handle changes of the surface of the gear. Cracks cannot be detected due to the rigid model. If, for example, a crack occurs for example in the tooth root, the tooth has to be able to bend in order to simulate the vibration behavior. This problem could be solved with flexible bodies. There are some issues that have to be solved in order to do a flexible body simulation. This is what this thesis is about. It continues the thoughts and analyses that have already be done and connects them to a significant industry problem, such as the wind turbine gearboxes with an extended level of complexity and application.

2 WIND TURBINE ENERGY CONVERSION

In the following chapter an **introduction to wind turbines** is presented in 2.1. Additionally the **theory for maximum energy generation** for wind turbines is explained in 2.2 and the **practical power generation of wind turbines** will be elucidated in 2.3, illustrated by the Nordex N90 wind turbine.

2.1 Introduction to Wind Turbines

There are several different kinds of wind turbine systems available. The main distinction is the orientation of the rotational axis. **Figure 2-1** shows a vertical orientation of a Darrieus system. There are many systems like that installed around the world. However, by far the most dominate system to convert the kinetic energy of the wind into electrical energy is the horizontal orientated axis system as seen in **Figure 2-2.**

Figure 2-1: Darrieus wind turbines
(Reference [18])

Figure 2-2: Typical horizontal axis wind turbine
(Reference [1])

These “typical” wind turbines are used all over the world to create emission free energy. In this elaboration, horizontal orientated wind turbines will be considered for further analysis. Wind turbine technology developed very fast in the last 40 years. Systems in the 1980’s could rarely produce more than 100kW. However, today’s system can now generate more than 5000kW[13]. The wind turbines run at a minimum wind speed of about 3 m/s and reach their rated power at around 14m/s. Wind turbines generally turn off at a wind speed of around 25 m/s for security

[13] Reference [2, p. 273]

reasons. The wind power plant is controlled by limiting, which can be controlled, for example by adjusting the blade angles (pitch control)[14].

Figure 2-3 shows the main parts of these kind of wind turbines. The parts can be divided into four main groups; rotor, energy conversion, sensors & structure and electric gear as shown in **Figure 2-4**.

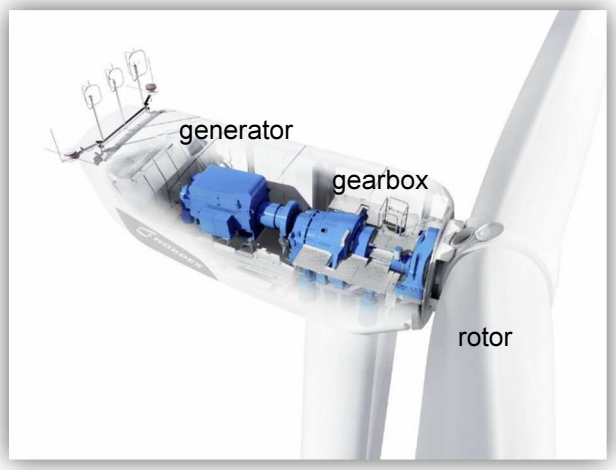

Figure 2-3: Typical megawatt wind turbine
(Reference [1])

Most of these systems are made of a rotor with three wing-shaped blades that are attached to a hub. The hub is attached to the nacelle, which houses the energy conversion and the sensors and structure parts.

[14] Reference [22, p. L 29]

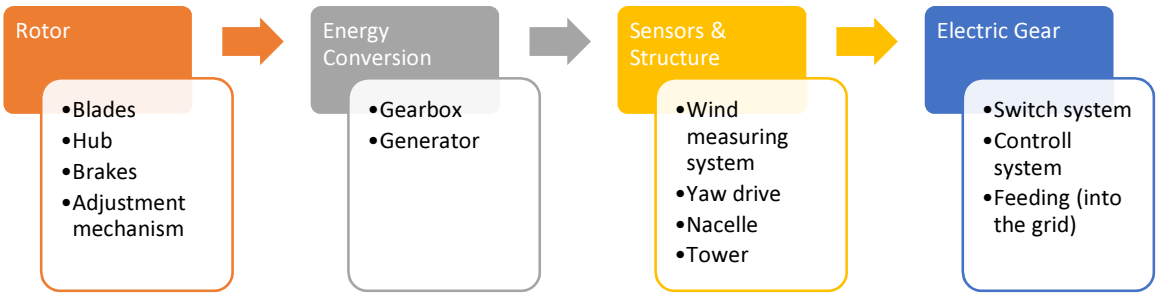

Figure 2-4: Four groups of main parts of a wind turbine[15]

The shaft of the rotor which is called low speed shaft is attached to the gear box. The gearbox increases the speed of the shaft from about 25-60 rpm to 1000-1800 rpm which is the rotational speed required by most generators to produce electricity[16]. This high speed shaft is connected to the generator via a brake system. Actual wind turbines are designed to work most efficiently at wind speeds of 8-11 m/s (18-24 mph) and generate their maximum power at 11-24 m/s (24-54 mph). To operate most effectively, the wind turbine adapts itself to the prevailing wind speed. It does this automatically by adjusting the blade speed. This can be done through breaking of the shaft, adjusting the blade angle or by turning the nacelle with a computer-controlled yaw system.

2.2 Theory for maximum Energy generation for wind turbines

Not all energy that is in the wind can be converted into mechanical energy and finally into electric energy. Therefore it is necessary to know what torque (input force for the mechanical system) reacts at the rotor at certain speeds due to the wind.

To determine the input force of the rotor of the wind turbine, the first step is to determine the kinetic energy E_{kin} of the air mass m_{air} which is passing the blades with a velocity v_{air}:

$$E_{kin} = \frac{1}{2} * m_{air} * {v_{air}}^2 \qquad (2\text{-}1)$$

[15] Reference [2, p. 273]

[16] For the connection to the main grid with an optimal efficiency

Looking at a specific cross-sectional area A_{rot} (in this case the rotor covered area), which is traversed with air at a certain velocity v_{air}, the traversed volume over time is the volume flow rate $\dot{V}_{air}$:

$$\dot{V}_{air} = v_{air} * A_{rot} \tag{2-2}$$

Considering the density of air ρ_{air}, the mass flow rate $\dot{m}_{air}$ is then:

$$\dot{m}_{air} = \rho_{air} * v_{air} * A_{rot} \tag{2-3}$$

Using an approach of looking at the kinetic energy of the moving air and the mass flow, leads to the traversed energy per time unit. A quantity of energy per time is physically identical to the power P:

$$P = \frac{1}{2} * \rho_{air} * {v_{air}}^3 * A_{rot} \tag{2-4}$$

The problem is figuring out how much mechanical power can be withdrawn from the air stream. Since the withdraw of mechanical power is only possible at the expense of the kinetic energy contained in the wind flow, the speed behind the wind turbine must decrease considering a constant mass flow rate. The reduction in the velocity also means a widening of the cross-section because the same amount of mass has to pass through, see **Figure 2-5**. It is therefore necessary to consider the states before and behind the wind turbine.

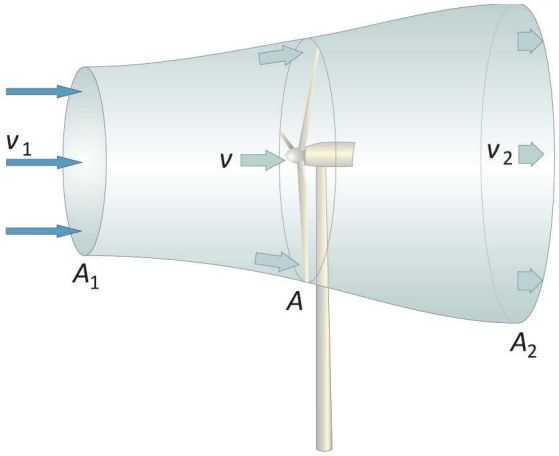

Figure 2-5: Widening of the cross-section
(Reference [2, p. 264])

Therefore, v_1 is the velocity of air before the rotor (not delayed) and v_2, the velocity behind the rotor (delayed). The mechanical power P generated by the wind turbine due to detraction of

energy of the air stream, correlates with the performance difference of the air stream before and behind the rotor[17]:

$$P_N = \frac{1}{2} * \rho_{air} * {v_1}^3 * A_1 - \frac{1}{2} * \rho_{air} * {v_2}^3 * A_2 \quad (2\text{-}5)$$

Hence, the continuity equation says about the mass flow rate,

$$\rho_{air} * v_1 * A_1 = \rho_{air} * v_2 * A_2 \quad (2\text{-}6)$$

therefore,

$$P_N = \frac{1}{2} * \rho_{air} * v_1 * A_1 * ({v_1}^2 - {v_2}^2) = \frac{1}{2} * \dot{m}_{air} * ({v_1}^2 - {v_2}^2) \quad (2\text{-}7)$$

The speed at the rotor v_{air} can be determined though the median of v_1 and v_2,

$$v_{air} = \frac{1}{2} * (v_1 + v_2) \quad (2\text{-}8)$$

therefore,

$$\dot{m}_{air} = \rho_{air} * A_{rot} * v_{air} = \rho_{air} * A_{rot} * \frac{1}{2} * (v_1 + v_2) \quad (2\text{-}9)$$

therefore the mechanical power P generated by the wind turbine,

$$P_N = \frac{1}{4} * \rho_{air} * A_{rot} * (v_1 + v_2) * ({v_1}^2 - {v_2}^2) \quad (2\text{-}10)$$

To compare the energy that is converted with the energy that could be converted, the power coefficient c_p is introduced. Hence, it is necessary to calculate the energy as if there would be no power transformation at the rotor. The power due to the kinetic energy would be the same at all locations,

$$P_0 = \frac{1}{2} * \rho_{air} * A_{rot} * {v_1}^3 \quad (2\text{-}11)$$

The power coefficient c_p is defined as,

$$c_p = \frac{P_N}{P_0} = \frac{1}{2} * (1 + \frac{v_2}{v_1}) * (1 - \frac{{v_2}^2}{{v_1}^2}) \quad (2\text{-}12)$$

Just for analyzing purposes a variable H will be defined,

[17] Reference [2]

$$\mathrm{H} = \frac{v_2}{v_1} \tag{2-13}$$

Which leads to a curve as shown in **Figure 2-6.** This curve shows the power coefficient c_p in relation to $\mathrm{H} = \frac{v_2}{v_1}$. The power coefficient c_p which shows the ideal power conversion, can be maximized for a certain ratio of the velocity of air before the rotor v_1 (not delayed) and the velocity behind the rotor v_2 (delayed).

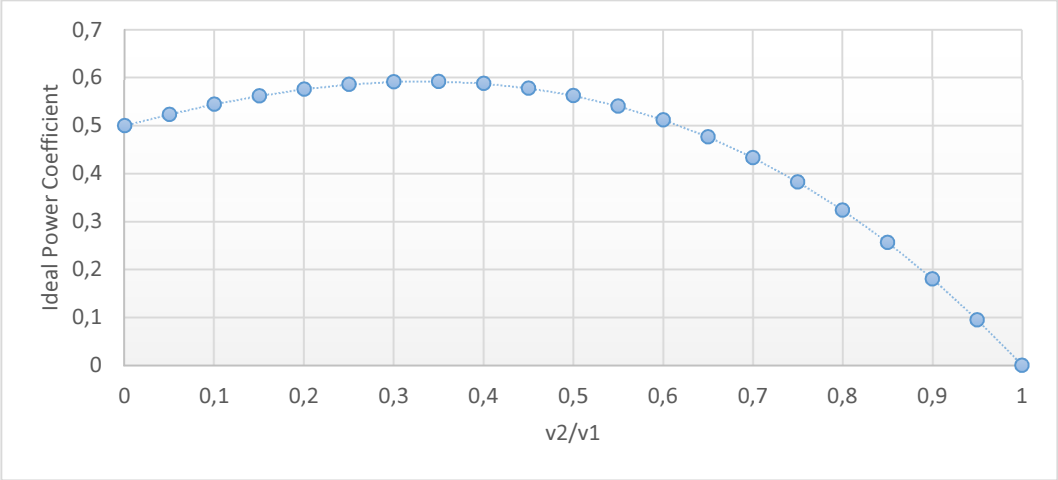

Figure 2-6: Power coefficient over ratio of wind speeds

Then c_p can be maximized at $\frac{\partial c_p}{\partial \mathrm{H}} = 0$,

$$\frac{\partial c_p}{\partial \mathrm{H}} = \frac{\partial(\frac{P_N}{P_0})}{\partial \mathrm{H}} = -\frac{3}{2} * \mathrm{H}^2 - \mathrm{H} + \frac{1}{2} = 0 \tag{2-14}$$

$$\mathrm{H} \approx \frac{1}{3} \tag{2-15}$$

$$c_{p,Betz} = 0.593 \tag{2-16}$$

The theoretical most effective power coefficient is therefore, $c_{p,Betz} = 0.593$ at a ratio of $\mathrm{H} = \frac{v_2}{v_1} \approx \frac{1}{3}$.

2.3 Practical Power generation in wind turbines (Nordex N90)

For practical wind turbines the power coefficient c_p for the different wind speeds v_{air} defines the behavior of the system. Meaning how much of the kinetic wind energy can be converted into mechanical energy P_N with the current rotor system. Therefore the behavior of the system can be described by the power coefficient c_p at certain wind speeds v_{air}. **Figure 2-7** shows the power coefficient c_p of a Nordex N90 2.3kW wind turbine. Nordex N90 wind turbines are installed in the "Highland" wind farm in Pennsylvania, USA[18] in 2008 and in Gut Losten, Germany in 2004 as well as many other places around the world.

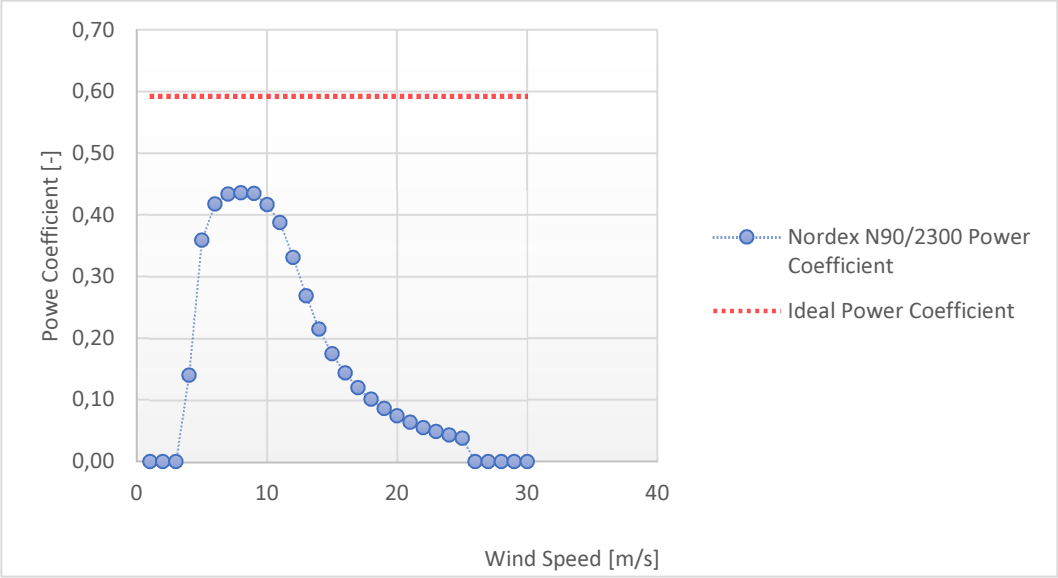

Figure 2-7: Power coefficient curve of a Nordex n90/2300 wind turbine
(Based on data from reference [3])

The efficiency η of a wind turbine system is defined as,

$$\eta = \frac{c_p}{c_{p,Betz}} \tag{2-17}$$

Meaning, how much of the theoretical possible kinetic energy can be converted into mechanical energy. Hence, the efficiency η is not a very interesting factor for wind turbine design. It may be an indicator about how "well designed" the system is from an engineering perspective. But it is much more of interest how much Power P_N can be generated at a certain wind speed v_{air}.

[18] Reference [21, p. 24]

Because the Power P_N is the factor that returns the investments. The generated Power P_N can be calculated based on the information of the power coefficient c_p, wind speeds v_{air}, density of air ρ_{air} as well as the covered area of the rotor A_{rot}:

$$P_N = c_p * P_0 = c_p * (\frac{1}{2} * \rho_{air} * {v_{air}}^3 * A_{rot}) \quad (2\text{-}18)$$

Table 2-1 shows the power coefficient c_p and the calculated generated Power P_N of a Nordex N90/2300 wind turbine system with a rotor diameter of 90m and an air density of $\rho_{air} = 1.295\ \frac{kg}{m^3}$.

Table 2-1: Nordex N90/2300 spec sheet [3]

Wind speed v_{air} [m/s]	**Power Coefficient c_p [-]**	**Power P_N [kW]**	**Efficiency η [-]**
4	0.140	35	0.24
5	0.359	175	0.61
6	0.418	352	0.70
7	0.434	580	0.73
8	0.436	870	0.74
9	0.435	1,237	0.73
10	0.417	1,623	0.70
11	0.388	2,012	0.65
12	0.331	2,230	0.56
13	0.269	2,230	0.45
14	0.215	2,230	0.36
15	0.175	2,230	0.30
16	0.144	2,230	0.24
17	0.120	2,230	0.20
18	0.101	2,230	0.17
19	0.086	2,230	0.15
20	0.074	2,230	0.12
21	0.064	2,230	0.11
22	0.055	2,230	0.09
23	0.049	2,230	0.08
24	0.043	2,230	0.07
25	0.038	2,230	0.06

Based on the Power P_N the Torque T_N can be calculated,

$$T_N = P_N * \omega \quad (2\text{-}19)$$

Figure 2-8 shows the Power P_N and the Torque T_N of a Nordex N90/2300 unit for the different wind speeds v_{air}.

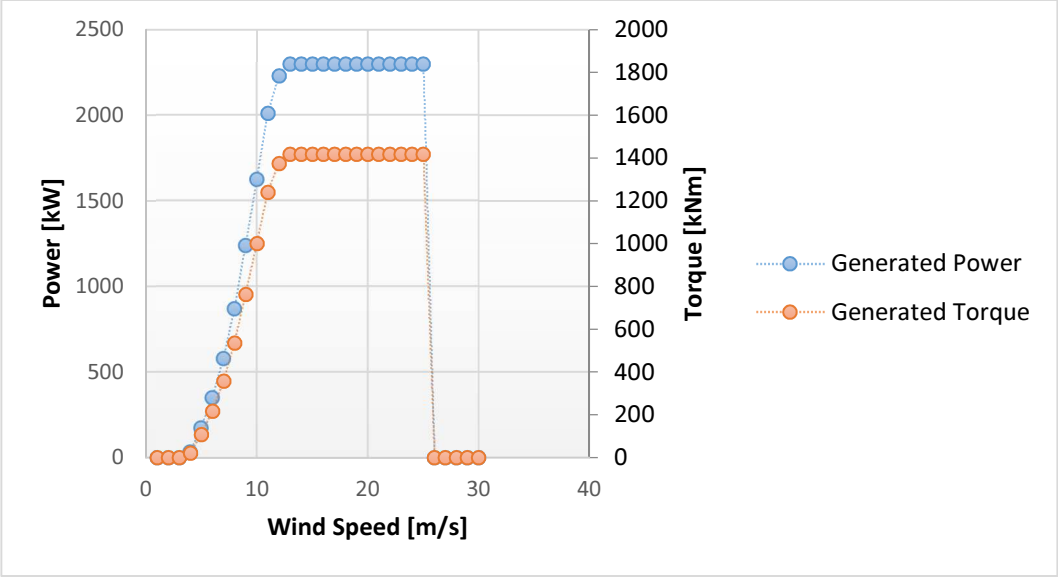

Figure 2-8: Power and torque related to the wind speed

This torque curve can be used as an input function in a multi body dynamics simulation model for a certain characteristic of a wind curve.

3 GEAR FAILURE

Chapter 3 provides an overview about the **gear failure modes** in 3.1. These failure modes will be related to the gear box in **frequency of failure modes of wind turbines** in 3.2. Followed by a short section about **load influence factors** in 3.4. Furthermore an insight of the **contact and forces at the tooth of the gear** will be given in 3.3 as well as information about the **tooth root load capacity** in 3.4.

3.1 Gear Failure Modes

According to industrial standards[19] the cases for breakage and fatigue of gear teeth can be divided into Tooth breakage and Tooth flank failure as shown in **Figure 3-1**. Wind turbines should not stand still over a long time because fretting corrosion[20] can occur. Characteristics of the fretting corrosion are brown-red, irregularly thick, often paint-like coverings or powdery wear which is difficult to remove that occurs at the tooth flanks of gears.

[19] Reference [7]

[20] Reference [7, p. 5]

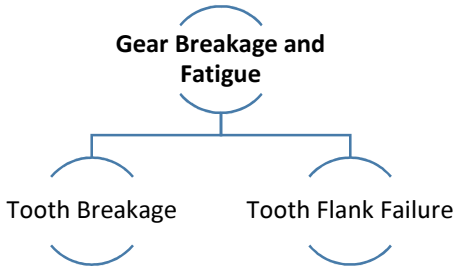

Figure 3-1: Breakage and fatigue of gear teeth

3.1.1 Tooth breakage

The breakage of a tooth (see **Figure 3-2** and **Figure 3-3**) is in general the end of the lifetime of a gear. Especially hardened teeth break completely or partly. These breakages occurs mostly at the tooth root (**Figure 3-2**) of the teeth if the application stress exceeds the tolerable load of the gear. Less common are flank breakage (**Figure 3-3**) on the loaded flank. The reason for the failure due to breakage can be fatigue breakage (due to material fatigue) or overload breakage (due to excessive bending loads of the tooth root).

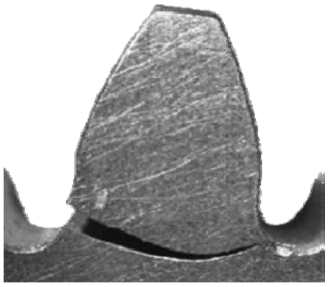

Figure 3-2: Typical tooth root breakage
(Reference [23, p. 2])

Figure 3-3: Typical tooth flank breakage
(Reference [23, p. 2])

A parameter that shows the capacity of a tooth is the modified allowable tooth-root stress limit σ_{FG} which is defined by the nominal stress number (bending) σ_{Flim} and two safety factors, lifetime factor Y_{NT} and size factorY_X.

For more information about the tooth load and load capacity of the tooth flank and the verification see chapter 4.7 on page 30.

Fatigue breakage (**Figure 3-4**) takes place in three stages: crack initiation, propagation and fracture.

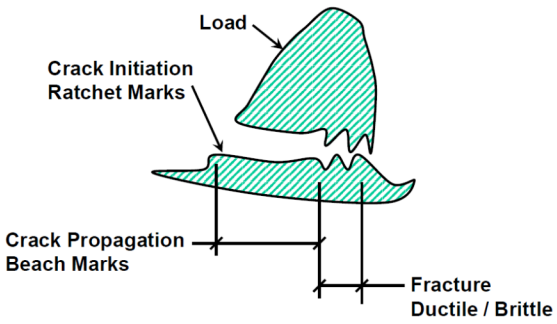

Figure 3-4: Fatigue breakage
(Reference [4, p. 3])

Step 1, crack initiation

During stage 1, local plastic deformation occurs in regions of stress concentrations or areas of discontinuities. In this stage micro cracks inside the grains follow.

Step 2, propagation

The cracks turns and grows perpendicular to the maximum tensile stress across the grain boundaries. Plastic deformation is confined at small zones at the leading edge of the crack. However there are no obvious signs of gross plastic deformation visible. This makes it hard for the maintenance personal to detect bending fatigue during step 2.

Step 3, fracture

Characteristic for bending fatigue is a sudden fracture during stage 3. It can be single (ductile, brittle) or mixed-mode depending upon material properties and the applied stress.

This thesis will show ways to detect these kinds of breakage, with a simulation of a gear system, before step 3 happens.

Figure 3-5 shows the surface of a tooth failure due to fatigue breakage. It shows the crack origins of the cracks as well as the propagation step, where the crack grows (beach marks).

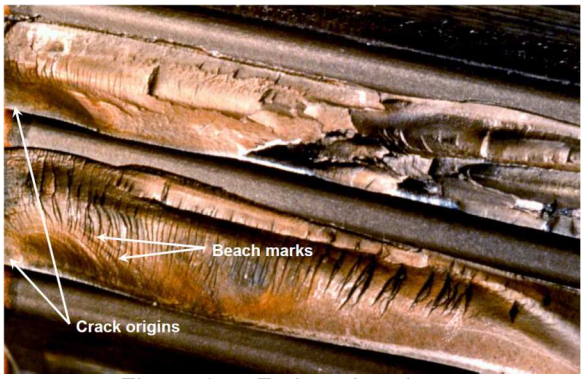

Figure 3-5: Fatigue breakage
(Reference [4, p. 5])

Reasons for bending fatigue can be overload of the gear tooth or inclusion inside the gear material. **Figure 3-6** and **Figure 3-7** show the surface of a failed gear tooth due to inclusion.


Figure 3-6: Inclusion origin on tooth fragment
(Reference [4, p. 10])

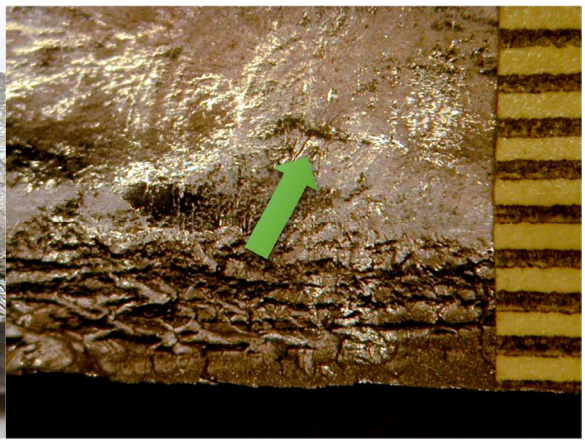
Figure 3-7: Close-up of origin
(Reference [4, p. 11])

3.1.2 Tooth flank failure

Tooth flank failure includes all damages of the gear that occur on the flanks of the gear teeth. Hence, it does not include a tooth breakage at the flank. This kind of damage is considered a tooth breakage and is discussed in chapter 3.1.1 on page 16. However, a tooth flank failure can lead to a tooth breakage.

If the tolerated stress of the tooth material is exceeded, particles of the material at the contact point can get loosen from the loaded tooth flank. With several rotations of the gear, these particles can generate pitting. These issues are common in gearboxes and reduces accuracy, creates noise and may lead to other issues. **Figure 3-8** shows an overview of failures that can occur on a wind turbine gear box.

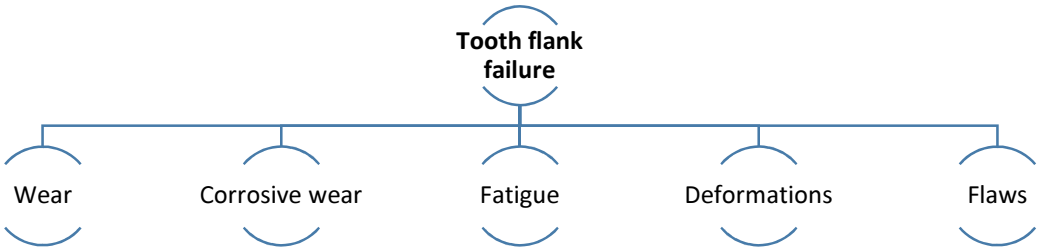

Figure 3-8: Overview of tooth flank failure

Tooth flank failures of wind turbine gear boxes includes failures like **wear** in **Figure 3-9** (normal wear, abrasive wear, interference wear, scratching scoring and scuffing) and **corrosive wear** in **Figure 3-10** (chemical corrosion, fretting corrosion, scaling ,overheating).

Figure 3-9: Wear (scuffing)
(Reference [5, p. 13])

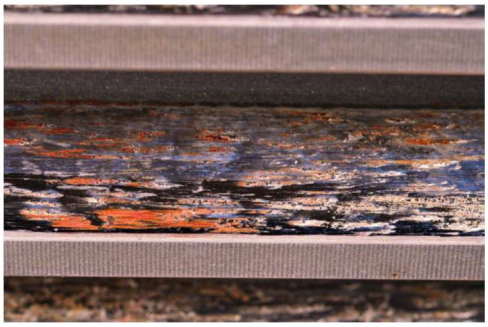

Figure 3-10: Corrosive wear (fretting corrosion)
(Reference [5, p. 17])

Further failures are flank **fatigue** in **Figure 3-11** and **Figure 3-12** (pitting, subcase fracture, spalling/chipping), **deformations** in **Figure 3-13** (indentations, rippling, rolling and peening, hot flow) and **flaws** in **Figure 3-14** (quenching cracks, hardening cracks, material flaws, grinding cracks, fatigue cracks).

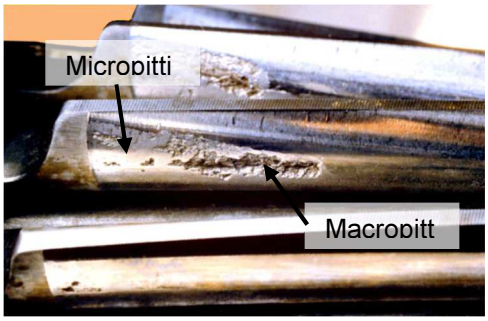

Figure 3-11: Flank fatigue (Pitting)
(Reference [4, p. 22+23])

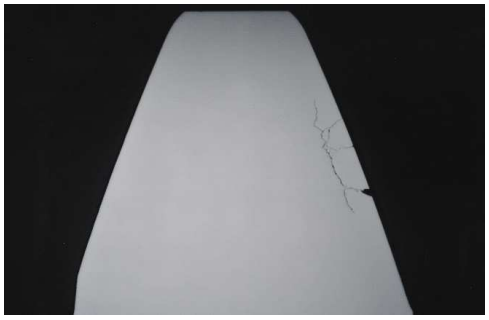

Figure 3-12: Flank fatigue (subcase fracture)
(Reference [6])

Figure 3-13: Deforamtion
(Reference [6])

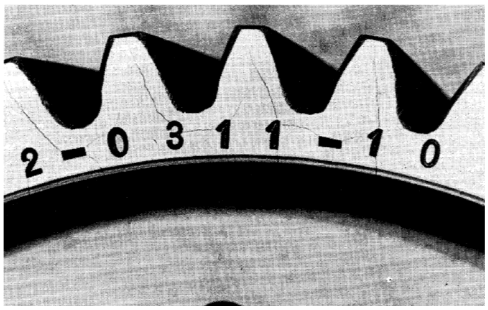

Figure 3-14: Flaws (hardening cracks)
(Reference [7, p. 13])

3.2 Frequency of Failure Modes of Wind Turbine Gears

Figure 3-15 shows failures of wind turbine gears. Most of the failures can already be simulated with rigid body elements in the Cal Poly Engineering department (Wear, Fatigue flank failure, Fracture or brittle due to overload). However, it shows that 27% percent of failures of wind turbine gears are due to cracks of the tooth. Rigid body elements cannot simulate theses failure types. Therefore this thesis handles the flexible body simulation of the cracked gear teeth. With the flexible and rigid body simulation most of the failure types can be simulated.

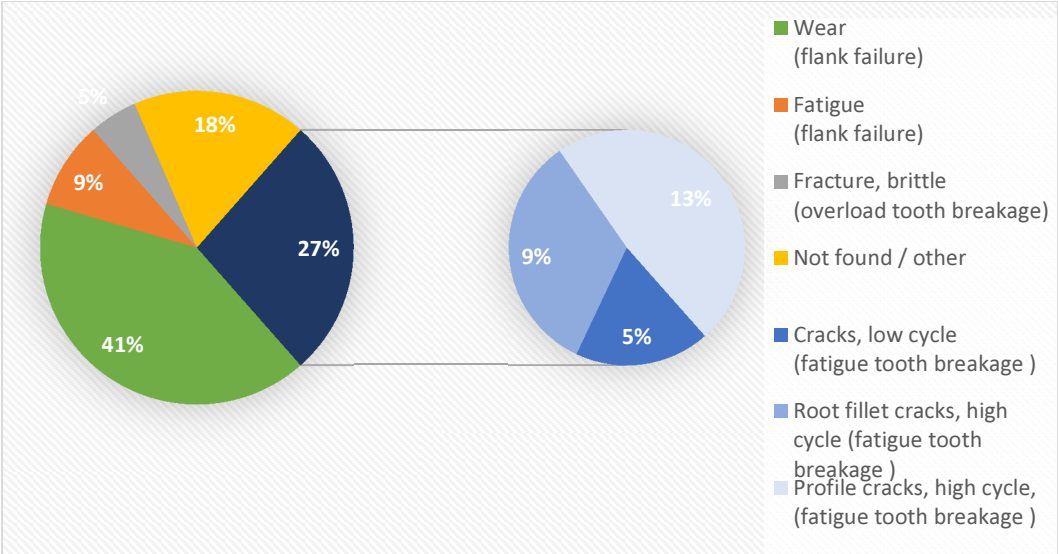

Figure 3-15: Recorded gearbox incidents summary from the NREL database
(Based on data from reference [8, p. 8])

3.3 Forces at the Tooth of the Gear

The worst case for the transmission force in gears is, when only one pair of teeth is in engagement. For a spur gear (β=0°) the tooth force is assumed to be a single force F_b. This force

is perpendicular to the surface at the contact point.[21] This can be represented as two forces, the tangential force F_t and the radial force F_r, as seen in **Figure 3-16**.

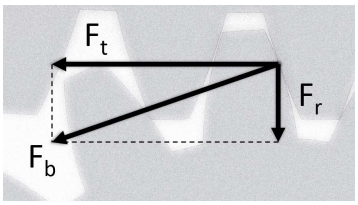

Figure 3-16: Tooth forces for spur gear (β =0°)

For a helical gear (β>0°) an axial force F_a will occur as shown in **Figure 3-17**. Hence, for a helical gear the tooth force F_{bn} is represented by three forces: tangential force F_t, radial force F_r and an axial force F_a.

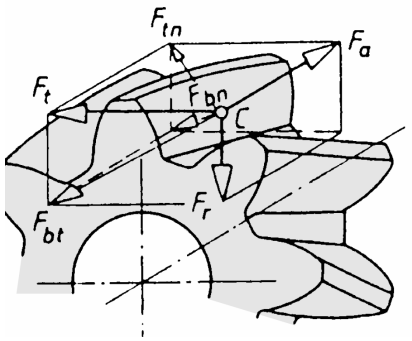

Figure 3-17: Tooth forces for spur gear (β > 0°) (Reference [9, p. 745])

For a given input torque T_{in} and a pitch diameter d of the gear the tangential force F_t can be calculated,

$$F_t = \frac{T_{in}}{0.5 * d} \qquad (3\text{-}1)^{22}$$

[21] Reference [9, p. 743]

[22] Reference [9, p. 745]

The radial force F_r can be calculated with the tangential force F_t, pressure angle α and helix angle β,

$$F_r = \frac{F_t * \tan \alpha}{\cos \beta} \qquad (3\text{-}2)^{23}$$

3.4 Factors of Load Influence

To calculate the forces of a meshed gear accurately, meaning as close as possible/necessary to reality, factors of load influence are added to the calculation. These factors are:

- Application Factor K_A

  (additional forces due to the drive and the gear, e.g. impacts and torque fluctuation)
- Internal Dynamic Factor K_v

  (force due the dynamic behavior of the system, e.g. deformations of the shaft)
- Transverse Load Factors $K_{F\alpha}$

  (characterizes effects of unevenly divided forces, if more teeth are in contact at the same time)
- Face Load Factor $K_{F\beta}$

  (characterizes effects of unevenly distributed force along the tooth width)
- Mesh Load Factor K_γ

  (characterizes the effect of multiple planets in a planetary gear)

These factors are based on results of researches and operating experience[24]. In chapter 4.7 on page 30 these factors have been applied for the planetary gear design of the wind turbine.

[23] Reference [9, p. 745]

[24] Reference [27]

3.5 Tooth Root Load Capacity

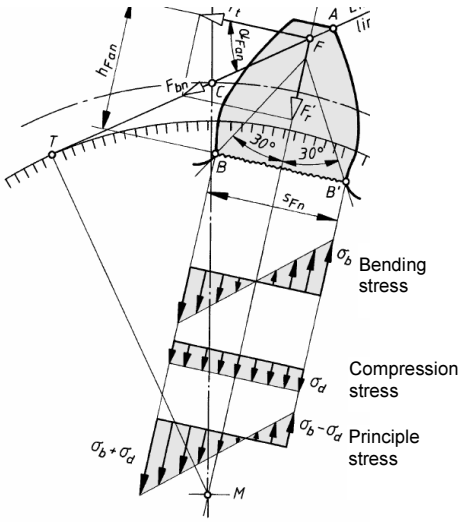

Figure 3-18: Tooth stress
(Reference [9, p. 704])

The tooth root is mostly endangered when the tooth force is acting at the top of the tooth.

Figure 3-18 shows the bending and compression stress at the tooth root. The considered cross section for the calculation is the rectangular section with the distance of BB'. The resulting force is the principle stress shown at the bottom Figure 3-18.

4 GEAR DESIGN FOR WIND TURBINES

This chapter explains the **design of planetary gears** in 4.1 and the **parts and structure of a standard planetary gear** in 4.2. Furthermore calculations for **the gear ratio & number of teeth for ring and sun gear** in 4.3, **the pitch diameters & number of teeth for planets** in 4.4 and the **design properties for planetary gears** in 4.5 will be shown.

These calculations are implemented in the **simplified guidance for planetary gear boxes of wind turbines** in 4.6 with the **strength and durability verification** in 4.7. Finally the **backlash of gears** in 4.8 and some application parameter as **power & torque** in 4.9 and **relative speeds** in 4.10 will be discussed.

4.1 Design of Planetary Gears

Planetary Gears can be applied in a lot of applications because of their good properties. These properties are coaxial shaft position of the input and output (round construction) and extremely low or high transmission in one or a few steps (forward and backward). This type of gear is used especially in the car and ship industry as well as in turbine and machine design. It is found in wind turbines around the world to generate climate friendly energy with the natural renewable resources that are provided on this planet.

The advantages of a planetary gear are manifold. It has a less sensitivity to shock loads and balance of static forces within the transmission system. One of the most positive properties is the distribution of torque and power on plurality of planet gears and power sharing between individual planetary gear sets. This results to smaller gears, smaller tooth speeds, smaller tooth forces (absolute), smaller dynamic tooth forces, small and compact design, low weight and favorable space power, smaller inertias and finally lower rolling and sliding speeds on the tooth flanks.[25]

[25] Reference [14, p. 19]

4.2 Parts and Structure of a Standard Planetary Gear

The standard planetary gear as shown in **Figure 4-1** consists of the *sun gear* (s), *planets* (p), *ring gear* (r) and the *carrier* (c). In a lot of applications, the ring gear is fixed to the frame. However it is possible to control the ring gear with an additional input speed or force. **Figure 4-2** shows a ring gear with additional external teeth. In this setup the sun gear *s* is in interaction with three planetary gears *p*, these are again in interaction with the ring gear *r*. The three planetary gears *p* are attached to the carrier *c* which receives the torque as the input motion.

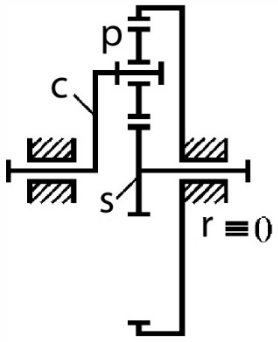

Figure 4-1: Simple planetary gear
(Reference [15])

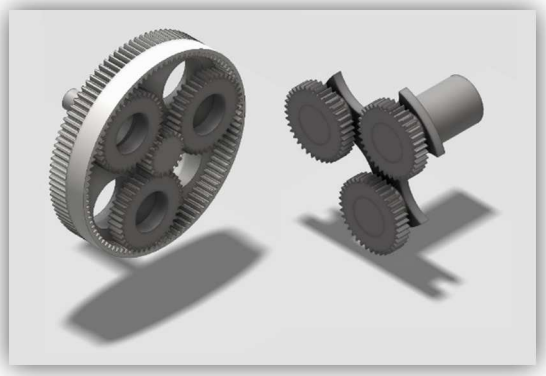

Figure 4-2: Planetary gear

4.3 Gear Ratio & Number of Teeth for Ring and Sun Gear

There are dependencies of the output speed of the gear that depend on the gear ratios of the transmissions. The gear ratio of the planetary gear system i is defined by the ratio of the number of teeth's of the ring gear z^r over the number of teeth's of the sun gear z^s:

$$i = i^{s,r} = 1 + \frac{z^r}{z^s} \tag{4-1}$$

This shows that the gear ratio of the planetary gear system i is not related to the number of the teeth of the planetary gears z^p. Furthermore the number of teeth of planetary gears do not have an influence to the gear ratio of the system. Hence, the number of teeth of the plenary gears z^p

are dependent of the teeth of the ring gear z^r and the teeth of the sun gear z^s as well as the module and the diameter of the ring and sun gear:

In cases of wind turbines, the maximum outer diameter for the ring gear is limited by the housing of the system. Hence, for the ring gear pitch diameter d^r is dependent of the outer diameter d^r_{max} and the thickness of the rim s_R as well as dedendum h_f (**Figure 4-3**).

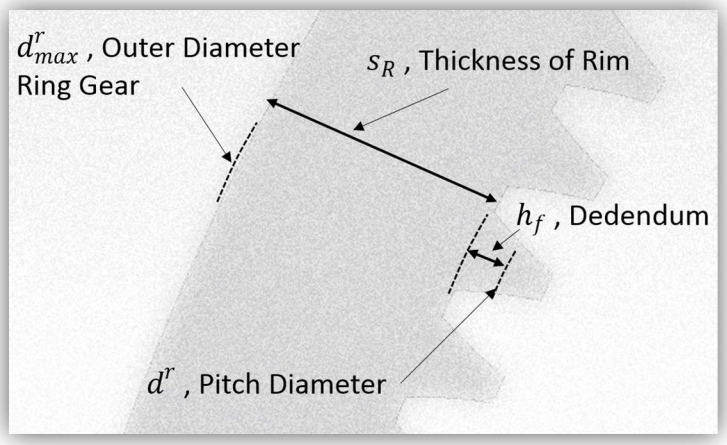

Figure 4-3: Ring gear notation

Therefor the pitch diameter d^r is:

$$d^r = d^r_{max} - 2 * (h_f + s_R) \quad (4\text{-}2)$$

$$d^r_{max} = \text{determined by gearbox housing} \quad (4\text{-}3)$$

$$h_f = m + c_p \quad (4\text{-}4)\ [26]$$

$$m = \text{defined from table}[27] \quad (4\text{-}5)$$

$$c_p = 0.1 \ldots 0.4 \quad (4\text{-}6)\ [28]$$

$$s_R = (3.5 \ldots 4.2) * m \quad (4\text{-}7)\ [29]$$

[26] Equation 21.5 – from reference [9, p. 712]

[27] Reference [16, p. 1]

[28] Chapter 4.4 – in reference [17, p. 2]

[29] Reference [9, p. 705]

For a given pitch diameter d^r , a defined helix angle β (in this thesis β =0) and a defined module m, the number of teeth's of the ring gear z^r can be determined.

$$z^r = \frac{d^r * \cos(\beta)}{m} \qquad (4\text{-}8)^{30}$$

Because of obvious reasons, the number of teeth of the ring gear has to be a whole number. That means that the calculated value has to be rounded. The corrected number of teeth of the ring gear z^{r*} leads to a corrected pitch diameter d^{r*}.

Henceforth, for the number of teeth of the ring gear z^{r*} and the necessary gear ratio of the planetary gear system i, the number of teeth of the sun gear z^s can be calculated with equation 4-1. This number has also to be a whole number, corrected number of teeth of the sun gear z^{s*}which also leads to corrected gear ratio of the planetary gear system i^*. If the corrected gear ratio is not sufficient, it can be influenced with the adjustment of certain parameters. An easy way is to change the module, whereby a smaller module general leads to smaller differences.

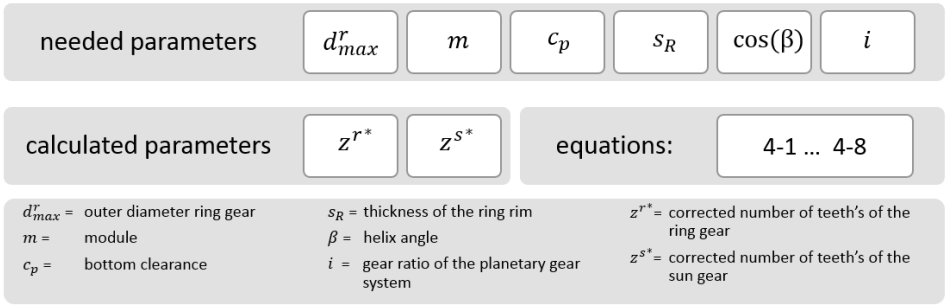

Figure 4-4: Summary of calculations from chapter 4.3

4.4 Pitch diameters & Number of Teeth for Planets

The pitch diameter for the ring gear can be calculated based on equation 4-8. Note, the corrected number of teeth of the ring gear z^{r*} with a whole number for the teeth has to be used. In the same way the pitch diameter d^{s*} can be calculated. For this the corrected pitch diameter d^{r*} and d^{s*} can be used for the gear modeling.

[30] Equation 21.38 - from reference [9, p. 728]

$$d^{r^*} = \frac{z^{r^*} * m}{\cos(\beta)} \quad and \quad d^{s^*} = \frac{z^{s^*} * m}{\cos(\beta)} \tag{4-9}$$[31]

Due to the geometry of a simple planetary gear, the pitch diameter of the planet d^p can be calculated by

$$d^p = \frac{d^{r^*} - d^{s^*}}{2} \tag{4-10}$$

With the pitch diameter d^p the number of teeth of the planet gear z^p can be calculated

$$z^p = \frac{d^p * \cos(\beta)}{m} \tag{4-11}$$[32]

For assembly purposes it may be interesting to know the center distance a_d of the center of the planets to the center of the sun and ring gear

$$a_d = \frac{d^p + d^s}{2} \tag{4-12}$$

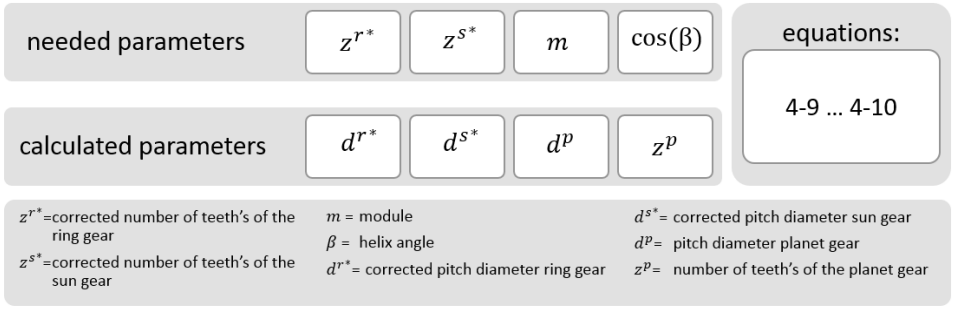

Figure 4-5: Summary of calculations from chapter 4.4

4.5 Design Properties for Planetary Gears

4.5.1 Necessary Design Properties

In order to assemble the gearbox successfully, it has to fulfill some design properties. To make sure that the sun, all planets and the ring gear mesh properly the following equations must be true, were z^s is the number teeth of the sun gear, z^p is the number of teeth of the planet gear and z^{r^*} is the number of teeth of the ring gear:

$$z^{s^*} + 2 * z^{p^*} = z^{r^*} \tag{4-13}$$

[31] Equation 21.38 – from reference [9, p. 728]

[32] Equation 21.38 – from reference [9, p. 728]

And were $\#p$ is the number of planets.

$$\frac{z^{s^*} + z^{r^*}}{\#p} = Initgrer \tag{4-14}$$

Furthermore the number of planets cannot exceed a certain value due to space limitations of the ring gear. Therefore the sum of the pitch diameters d^p of all planets have to be smaller than a perimeter of an assembly circle defined by the center distance a_d of the gears.

4.5.2 Preferred Design Properties

Beside the necessary design properties, there are some preferred design properties. The teeth at a gear contact mesh periodically. It depends on the number of teeth in the gears how theses mesh. It could be that one tooth of one gear will just be in contact with a few others in the other gear. On the other hand, if the gear is well designed, one tooth of one gear will be in contact with every tooth of the other gear. To operate with a well-designed gear the number of teeth of the two gears should not have a common divisor[33]. Furthermore, the maximum gear ratio should not exceed $i = 6$ to make sure that the involute gear tooth can roll on each other's surface properly[34].

4.6 Simplified Guidance for Planetary Gear Boxes of Wind Turbines

Figure 4-6 shows a simplified guidance that has been elaborated for the wind turbine gear design. (The full guidance is shown in the **Error! Reference source not found.** A). It is based on gear design standards according to the German industry standard "DIN" (Deutsche Industrie Norm). Later in this thesis a planetary gear will be analyzed which has been designed according to this guidance. The blue filled boxes are given values that have to be picked beforehand. They are defined by the environment and application of the gearbox. The green/grey filled boxes are calculated values.

[33] Reference [9, p. 739]

[34] Reference [9, p. 738]

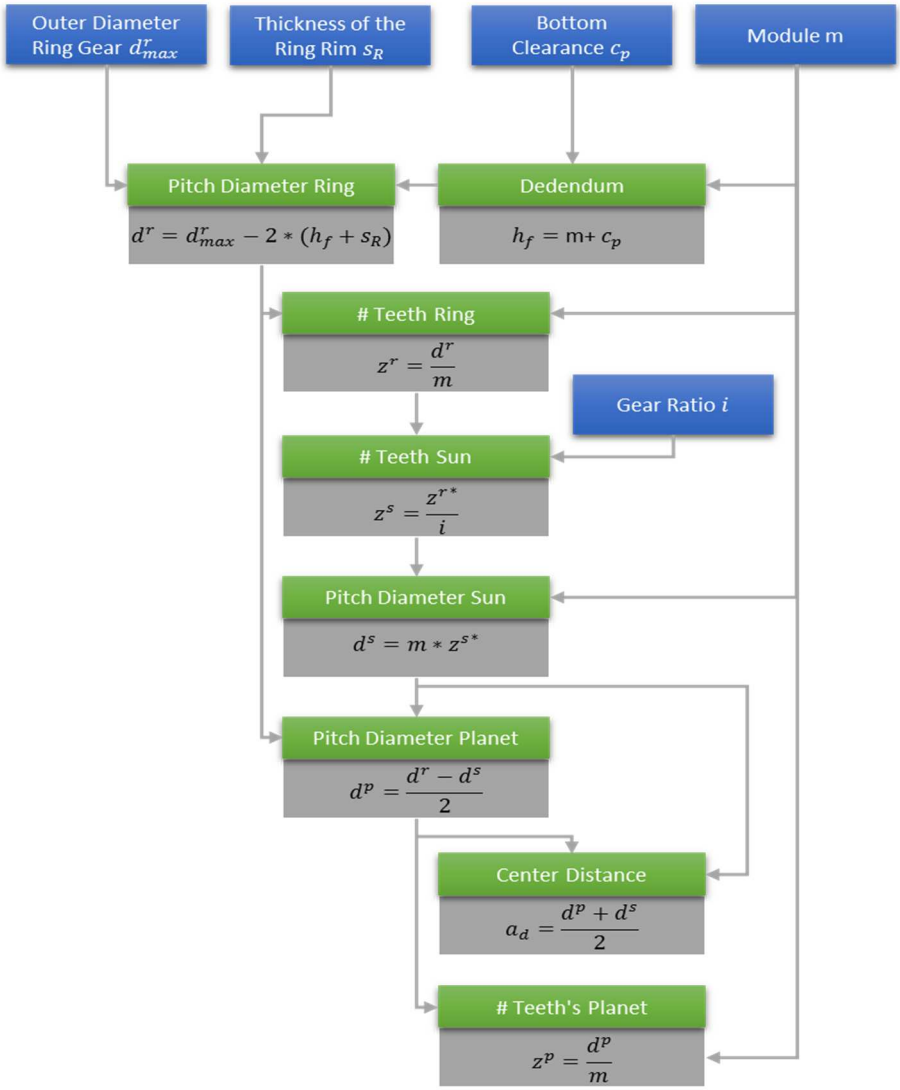

Figure 4-6: Simplified guidance for planetary gear boxes of wind turbines

4.7 Verification

With the usage of gears there are different kinds of stress. To make sure that the designed gears will satisfy the desired durability and strength, two different verification checks have to be passed:

- Tooth Strength
- Load Capacity of the Tooth Flank

These verifications, based on research and experience, make it possible to design the gear with a defined factor of safety. However, these parameters do not guarantee the desired gear life.

4.7.1 Tooth Strength Verification

The reasons for tooth breakage and the consequential tooth strength verification are described in chapter 3.1.1 on page 16. **Figure 4-7** shows the guidance that leads through the process. Starting with given values (blue filled boxes) which are given according to industry standards. The values are dependent on the environment, application and other parameter of the gear system. Additionally, the applied forces and design properties (blue framed boxes) are required values to verify the gear design. The interim results (light green filled boxes) lead to the verification equation (bright green box) that shows if the verification is successful.

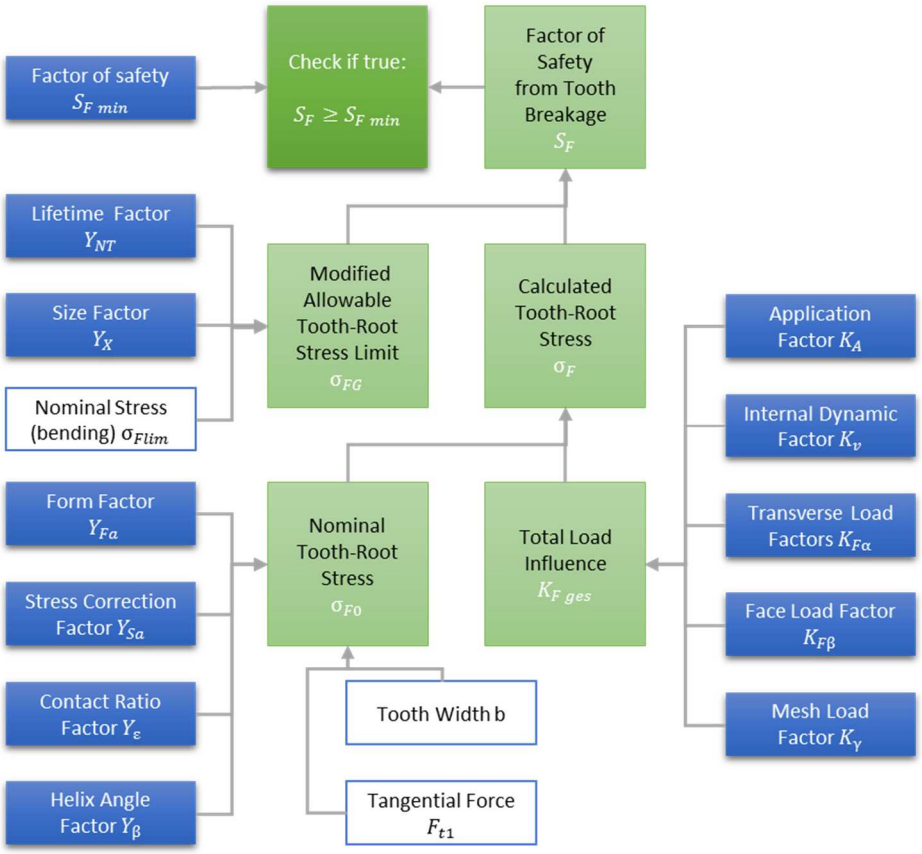

Figure 4-7: Tooth strength verification guidance

Table 4-1 shows references of given values (blue filled boxes) and interim results/ calculated values.

Table 4-1: Reference of given values (blue filled boxes)

Input Values	
Factor of Safety	Reference [9, p. 21.85]; 1.5 middle; >3 high risk high failure costs
Lifetime Factor	Reference [9, p. 751]
Size Factor	Reference [9, p. 751]
Form Factor	Reference [9, p. 750]; DIN 3990-3 Page 13; (Zn from Page 12); x=Profile Shift (addendum modification) in this case x=0
Stress Correction Factor	Reference [9, p. 750]; DIN 3990-3 Page 30; (Zn from Page 12); x= Profile Shift (addendum modification) in this case x=0
Contact Ratio Factor	Reference [9, p. 750]; DIN 3990-3 Page 38
Helix angle Factor	Reference [9, p. 750]; For Beta=0 DIN 3990-3 Page 39
Application Factor	Reference [9, p. 746]; DIN 3990-1 Page 55
Internal Dynamic Factor	Reference [9, p. 746]
Transverse Load Factors	Reference [9, p. 748]; DIN 3990-1 Page 47
Face Load Factors	Reference [9, p. 747]; DIN 3990-1 Page 39
Mesh Load Factor	IEC61400 Page 37
Interim Results/ Calculated Values	
Nominal Tooth-Root Stress	Equation 21.82 from reference [9]
Total Load Influence	Equation 21.81 from reference [9]
Calculated Tooth-Root Stress	Equation 21.83 from reference [9]
Modified Allowable Tooth-Root Stress Limit	Equation 21.84 from reference [9]
Factor of Safety From Tooth Breakage	Equation 21.85 from reference [9]; 1.5 middle; >3 high risk high failure costs

4.7.2 Load Capacity of the Tooth Flank Verification

The reasons for tooth flank failure and the consequential load capacity of the tooth flank verification are described in chapter 3.1.2 on page 18. The filling and frame colors of the boxes are the same as in chapter 4.7.1: Given values (blue filled boxes), applied forces and design properties (blue framed boxes), interim results (light green filled boxes) and the verification equation (bright green box).

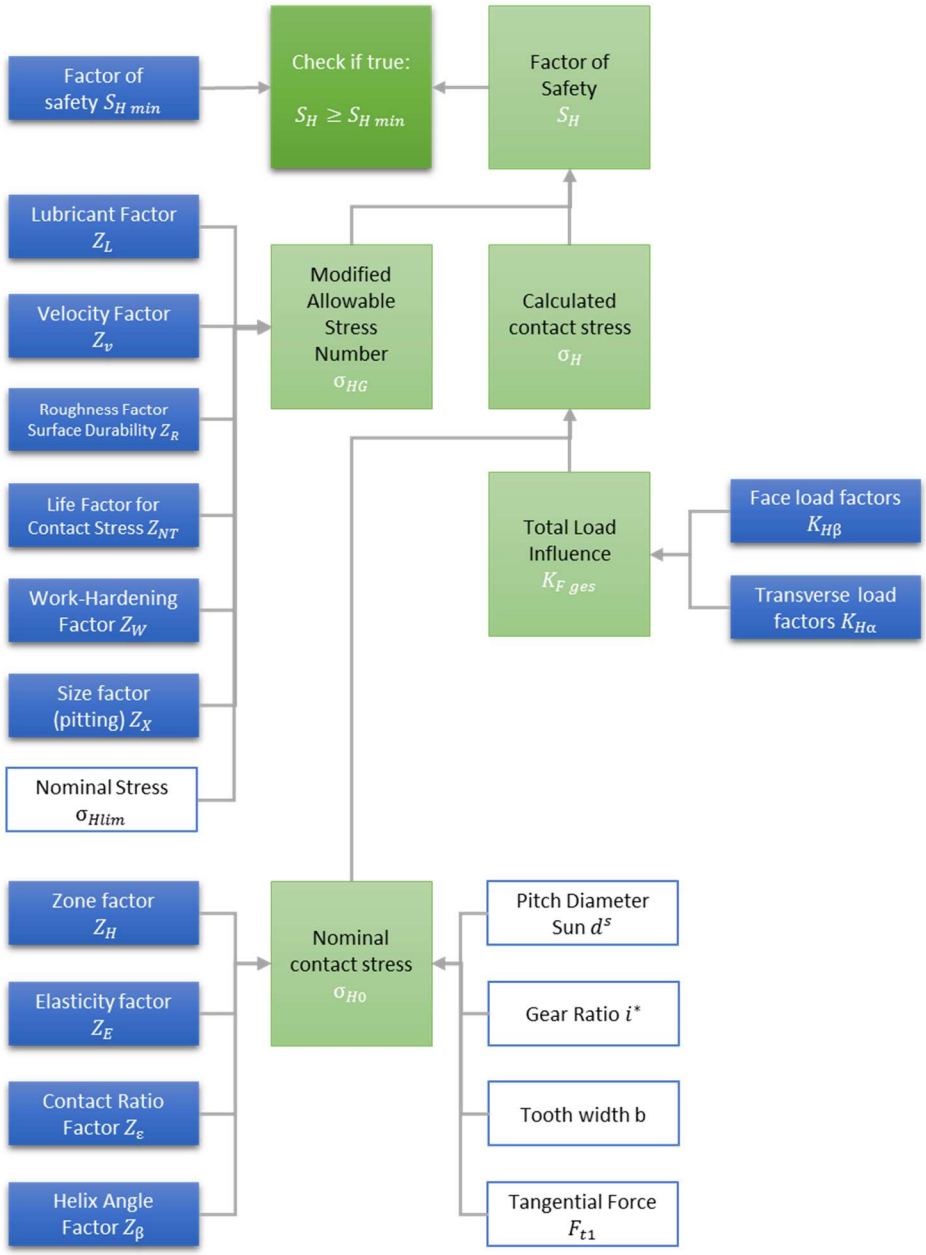

Figure 4-8: Load capacity of the tooth flank verification guideance

Table 4-2 shows references of given values (blue filled boxes) and interim results/ calculated values.

Table 4-2: Reference of given values (blue filled boxes)

Input Values	
Factor of Safety	Equation 21.90 from reference [9]; 1.0 …. 1.3 middle; >1.6 high risk high failure costs
Lubricant Factor	Reference [9, p. 754]
Velocity Factor	Reference [9, p. 754]
Roughness Factor Affecting Surface Durability	Reference [9, p. 754]
Life Factor for Contact Stress for Reference Test Conditions	Reference [9, p. 754]
Work-Hardening Factor	Reference [9, p. 754]
Size Factor (pitting)	Reference [9, p. 754]
Zone Factor	Reference [9, p. 753]
Elasticity Factor	Reference [9, p. 753]
Contact Ratio Factor (pitting)	Reference [9, p. 753]
Helix Angle Factor (pitting)	Reference [9, p. 753]
Transverse Load Factors	Reference [9, p. 748]
Face Load Factors	Reference [9, p. 747]
Interim Results/ Calculated Values	
Modified Allowable Stress Number	Equation 21.84 from [9]
Nominal Contact Stress	Equation 21.88 from [9]
Total Load Influence	Equation 21.81 from [9]

Calculated Contact Stress	Equation 21.89 from [9]

4.8 Backlash of Gears

The design of a gear pair with involute profile generates in theory a perfect meshing of the gears. Besides it is impossible to manufacture a perfect shape of the gear and a perfect meshing of the teeth, some disturbance can occur for heavy duty applications[35]. Even for simulations where a perfect gear shape and a perfect meshing can be generated, simulations errors occur due no backlash in the digital model. This leads to unexpected vibrations of the gear system. Real gears are manufactured with a specific backlash allowance due to the compensation of machining and assembly inaccuracies. Working conditions such as the lubrication and possible heat expansion during operation, are further reasons for the use of a backlash. This backlash ensures that just under sizing of the gear pair take place. By oversizing of the gear pair the gear cannot be assembled or the gear will get stuck which could lead to a completed failure of the gear system. To obtain the appropriate amount of backlash for spur gears two alternative ways are used by the industry today.

- Decreasing the tooth thickness
- Increase the center distance

Figure 4-9 shows the different ways to add backlash to a gear. The left side a) of the Figure 4-9 shows how to generate backlash by decreasing the tooth thickness due to Circular backlash j_t and Normal backlash j_n. The right side b) shows how to generate backlash by increasing the center distance of the gear pair due to center backlash j_r.

[35] Reference [20]

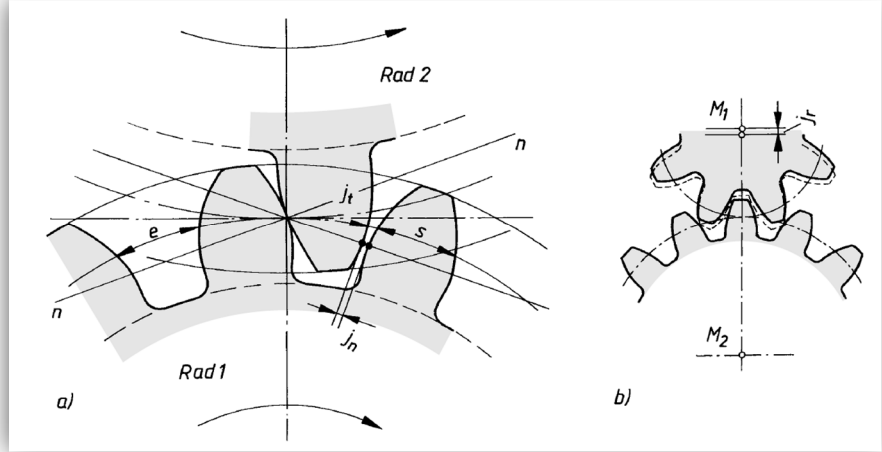

Figure 4-9: Backlash at gear teeth
(Reference [9, p. 734])

Circular backlash j_t: Is the distance of the working flank to the rear flank along the pitch circle, when the working flanks are in contact.

Normal backlash j_n: Is the shortest distance in normal direction between the rear flanks of the gear when the working flanks are in contact.

Center backlash j_r: Is the difference of the theoretical center distance (backlash-free) and the operating center distance.

A backlash which is too large will be result in additional stress and noise especially with changing of the force direction. If the amount of backlash is too small the system can be jammed. A recommended value[36] is $j_n = 0.05 + (0.025 \dots 0.1) * m_n$.

When designing a backlash, consider following factors[37]:

- Lubricant space required.
- Differential expansion between the gear components and the housing.
- Errors in machining, run-out of both gears, errors in profile, pitch, tooth thickness, helix angle and center distance. The smaller the amount of backlash, the more accurate the machining of the gears is.
- Working conditions such as frequent reversing or overrunning load.

[36] Reference [9, p. 734]

[37] Reference [13]

The value of the backlash does not indicate anything about the quality of the tooth, although the different qualities require certain dimensions of the tooth thickness[38].

4.9 Power & Torque

The main reason to use a planetary gear as a transmission, is the load splitting over the planets in a compact design. The input power P_{in} of a gearbox is related to the input torque T_{in} and the shaft speed ω_{in}:

$$P_{in} = T_{in} * \omega_{in} \tag{4-15}$$

The power/torque can be divided into several input power/torque forces at each planet. The carrier combines the power/torque forces again into one. Input power P_{in} and output power P_{out} of a planetary gear stage is defined through the efficiency factor,

$$P_{out} = P_{in} * \eta \tag{4-16}$$

However, the load is often assumed to be spitted evenly over each planet. This is not the case due to production tolerances and deformations of the gears. For the load calculation of the planetary gear a mesh load factor K_γ will be considered. This factor is defined for wind turbine system in IEC 61400-4 standard on page 37.

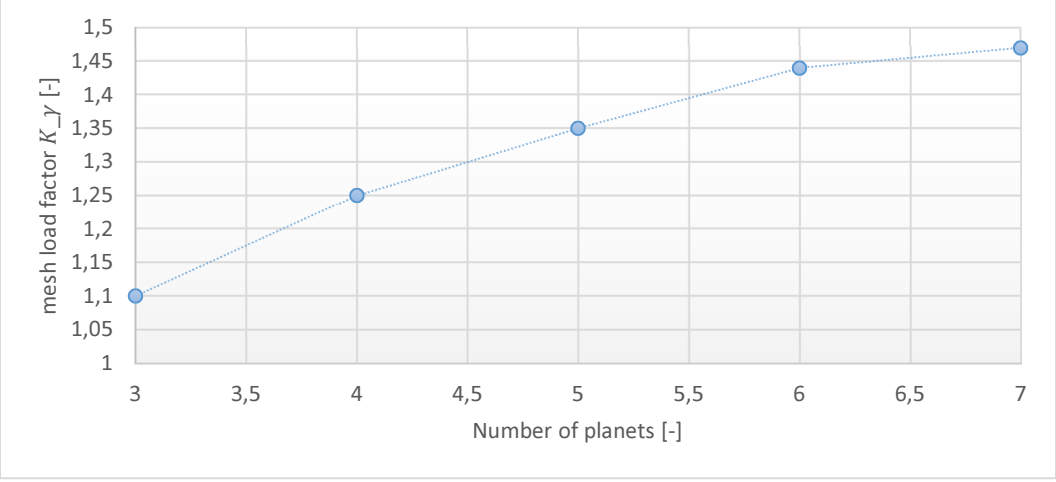

Figure 4-10: Mesh load factor K_γ

(Reference [10, p. 37])

[38] Reference [9]

The power at the planet $P^{P}_{verif.}$ for strength reliability verification is defined by the system input power P_{in} , the number of planets $\#p$ and the mesh load factor K_{γ},

$$P^{P}_{verif.} = \frac{P_{in}}{\#p} * K_{\gamma} \tag{4-17}$$

The mesh load factor K_{γ} will just be considered for the strength reliability verification and does not apply to the power distribution analysis of the gear box.

If there are higher deformations of the gear teeth the load splitting will be more even. Tests have shown that this assumption is true[39]. It indicates that the production tolerances lose their weight with higher deformations (higher forces).

4.10 Relative Speeds

The output speed of the sun gear n^{s} is the speed of the carrier n^{c} multiplied by the gear ratio of the planetary gear stage i (for i see equation 4-1):

$$n^{s} = n^{c} * i \tag{4-18}$$

The rotational speed of the planets is defined as,

for the joint itself

$$n^{p} = -\frac{z^{s}}{z^{p}} * (n^{s} - n^{c}) \tag{4-19}$$

and in respect of the center of the gear in consideration of the motion of the carrier,

$$n^{p} = -\frac{z^{s}}{z^{p}} * (n^{s} - n^{c}) - n^{c} \tag{4-20}$$

[39] Reference [26, p. 15]

5 MULTI BODY DYNAMICS SIMULATION IN MSC.ADAMS

In this chapter the multi body dynamics simulation in MSC.Adams is presented. This includes the **simulation process** in 5.1 which shows the steps that have been completed to achieve the results found in chapter 6. In 5.2 the **theory of the flexible bodies** is discussed. Running MBD gear simulations on a computer can take from several hours to days or weeks. For an analysis, hundreds of simulations have to be completed. Therefore the simulation setup should be done with a minimum of necessary computational resources. An important factor for minimizing the simulation time is the **simulation step size** in 5.3. In 5.4 the **stiffness value** and in 6.1 the **simulated system** will be discussed.

5.1 Simulation Process

To run a multi body dynamic simulation (**MBD**) several steps have to be completed. In MSC.ADAMS parts can be designed within the user interface. This works for simple geometries or parts that can be created with one of the many design tools that are provided. However, complex parts should be designed with Computer Aided Design (**CAD**) software. These parts can be imported into the MBD program. **Figure 5-1** shows the two steps for rigid body simulations. For flexible bodies two more steps have to be completed as shown in **Figure 5-2**.

To use flexible bodies in MSC.ADAMS a **.mnf** file is needed. There are only a few softwares available that can generate these files. In this thesis the “Abaqus Interface for MSC.ADAMS” has been used. The conversion interface requires input values that can be calculated with a modal analysis. The modal analysis can be calculated by an Finite Element Method (**FEM**) software, this study utilized Abaqus software.

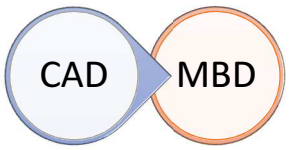

Figure 5-1: Simulation process for rigid bodies

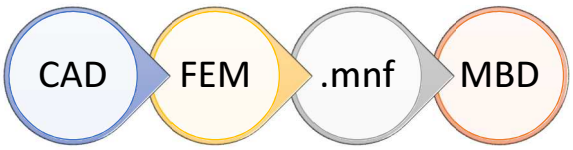

Figure 5-2: Simulation process for flexible bodies

5.1.1 CAD – AutoCAD Inventor

To model the gears for the N90/2300 gearbox, Autodesk Inventor Professional 2014 Student Version has been used. The involute profile of the gear has been designed with the spur gears component generator toolbox of Autodesk Inventor. All parameters were calculated in a Microsoft Excel sheet (see Appendix A: Gear Design Guide in Microsoft Excel) that was written according to the design process for planetary gears, see chapter 3 starting on page 15.

5.1.2 FEM – Abaqus

The FEM module generates a database for all nodes based on a modal analysis. This database determines the possible directions of motion of the flexible body nodes. The possible directions are determine by the natural mode shapes during free vibration of the system, called modal analysis. For more information about the modal analysis see chapter 5.2.1 on page 46.
Abaqus does not define any units for the user. Hence, the input value for the calculations has to be consistent and matching with each other. Units used in the thesis[40] are SI units [N, m, s, C, kg]
The material properties are shown in **Table 5-1**.

Table 5-1: Material properties of the simulated gear

NAME	VALUE
YOUNGS'S MODULUS	2.07E+11 N/m²
POISSONS RATIO	0.29 [-]
MASS DENSITY	7.8E+03 [N/m³]

Due to software and version compatibility problems, a script was written for the FEM calculation (see **appendix C**).

[40] Due to software limitations, SI units [N, m, s, C, kg] have to be used for MSC.Adams when importing data from Abaqus. Because N=kg*m/s² is always true, mm cannot be chosen for length in MSC.Adams.

This Script is divided into the following sub categories (for Abaqus version 6.13-2):

- Node definition
- Element definition
- Element property definition
- Material definition
- Modal analysis
- Substructure generation

5.1.2.1 Node definition

In order to keep the Input File clear, the definition of the nodes (which could be millions of lines) are written in a separate file. Node number 10000000 is a MPC reference node “BEAM” and is defined as “RETNODES” in a node set.

```
**  ----------------------------------------------
**
**                NODE DEFINITION
**
*NODE,input=Sun_nodes.inp
**
**
**                NODES SETS
**
*Nset, nset=Set-bc
     1,     2, …
**
**
**                MPC Definiton (Multi-point constraints)
**
*MPC
BEAM,Set-bc,10000000
**
**
*NSET, NSET=RETNODES
10000000
**  ----------------------------------------------
```

The MPC point constrains the single displacement degree of freedom node to the global displacements of the other nodes. In this case it connects the nodes on the surface of the bore (the shaft connection to the gear), with the reference node 10000000, which is located at the

center of the part. This reference node is the connection between the flexible gear and other rigid/flexible bodies in the MBD simulation later on. It indirectly connects the nodes on the surface of the bore to the spinning shaft.

5.1.2.2 Element, Element Property and Material Definition

The element definition is also written in a separate file to keep the INPUT file clear.

```
**  ----------------------------------------------
**
**                ELEMENT DEFINITION
**
*ELEMENT,TYPE=C3D8R,ELSET=PROP1,INPUT=Sun_elements.inp
**
**
**  ----------------------------------------------
```

```
**  ----------------------------------------------
**
**                ELEMENT PROPERTY DEFINITION
**
*SOLID SECTION,ELSET=PROP1,MATERIAL=STEEL
**
**  ----------------------------------------------
```

```
**  ----------------------------------------------
**
**                MATERIAL DEFINITION
**
*MATERIAL,NAME=STEEL
*ELASTIC
 2.07E+11, 0.29
*DENSITY
 7.8E-06,
**
**
**  ----------------------------------------------
```

5.1.2.3 Modal Analysis

In this section the frequency step is defined as well as the number of desired mode shapes.

Furthermore, the boundary conditions and the desired output of the calculation is set.

```
**  ----------------------------------------------
**
**               MODAL ANALYSIS
**
*STEP, name=frequency
*FREQUENCY,EIGENSOLVER=LANCZOS
20,
**
** BOUNDARY CONDITIONS
**
*BOUNDARY
RETNODES, 1,6
**
**
*ELEMENT MATRIX OUTPUT, MASS=YES, ELSET=PROP1
*NODE FILE
U
*END STEP
**
**  ----------------------------------------------
```

5.1.2.4 Substructure Generation

This section creates the substructure step. Boundary conditions for the substructure are defined as well as the number desired mode shapes. At the end, the desired output of calculation is set.

```
**  ----------------------------------------------
**
**               SUBSTRUCTURE GENERATION
**
*STEP
*SUBSTRUCTURE GENERATE, TYPE=Z1, RECOVERY MATRIX=YES,
 MASS MATRIX=YES, FLEXIBLE BODY, OVERWRITE
*RETAINED NODAL DOFS, SORTED=NO
RETNODES, 1,6
*SELECT EIGENMODES,generate
1,20,1
*SUBSTRUCTURE MATRIX OUTPUT, STIFFNESS=YES, MASS=YES,
 RECOVERY=YES
*END STEP
```

5.1.3 MNF – Abaqus Interface for ADAMS

The “Abaqus interface for ADAMS” converts the results of the modal analysis into a database that can be read by MSC.Adams. The MNF file generation is done by the software without any further changes of the files if the script for the modal analysis for Abaqus was written properly. **Figure 5-3** shows the Command window.

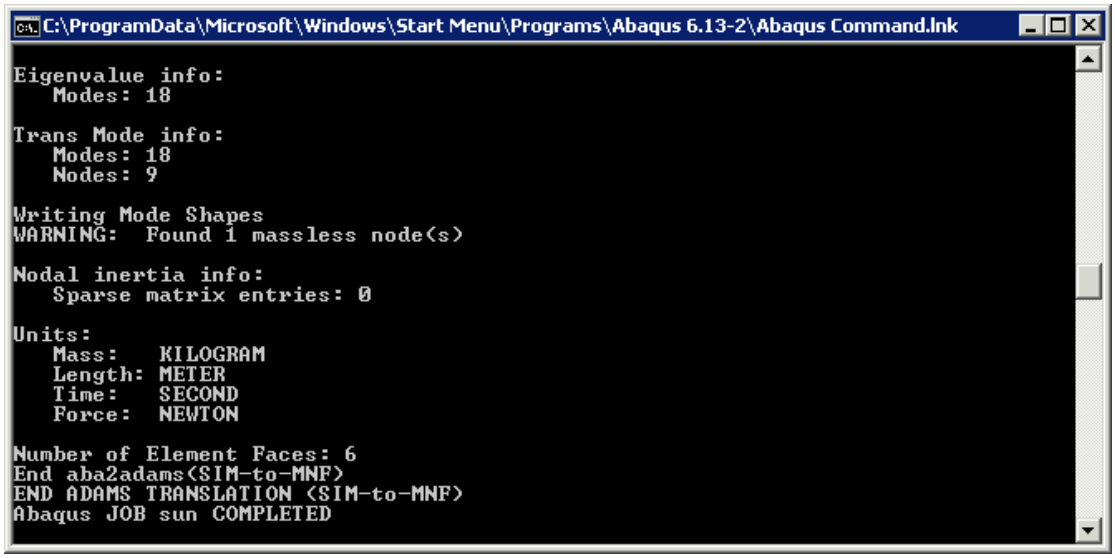

Figure 5-3: Command window of the Abaqus interface for ADAMS

5.1.4 MBD – MSC.Adams

Multi body dynamic (MBD) simulation is a system that consists of solid bodies that are connected to each other by joints. The bodies can interact with each other due to force/contact connections. It is a study of the influence of forces, like contact forces, gravity or other forces, that makes it possible to analyze the systems mechanism as motion and behavior. The MBD simulation was performed with MSC.Adams, **Figure 5-4** shows the user interface.

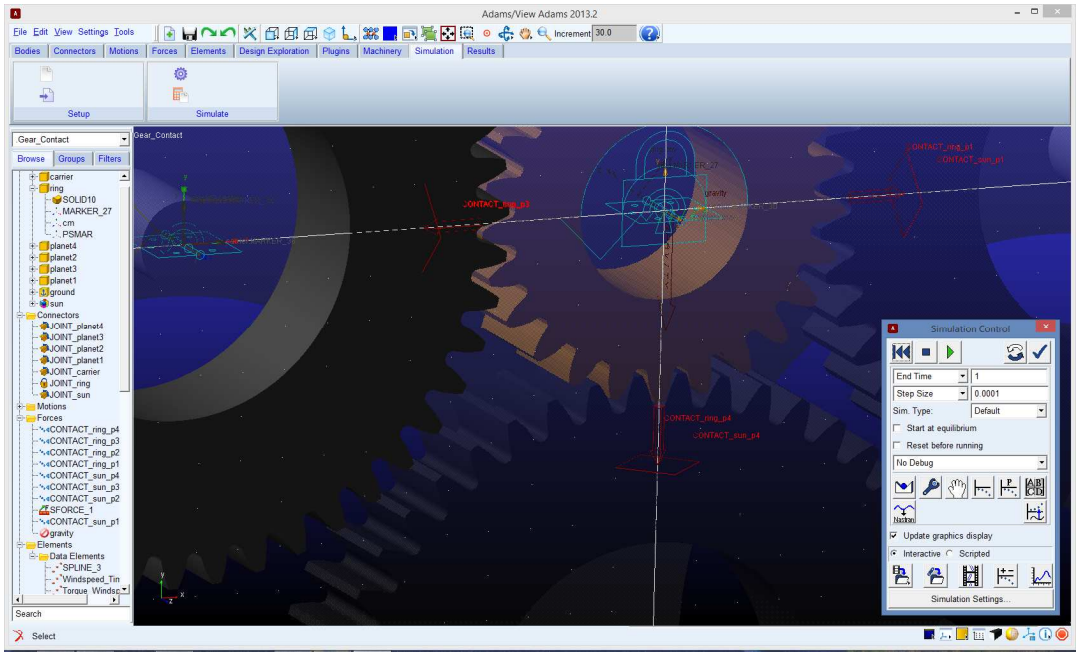

Figure 5-4: User interface MSC.Adams

Figure 5-5 shows a mode of the flexible body in MSC.Adams and **Figure 5-6** shows the deformation of a crocked tooth during a contact.

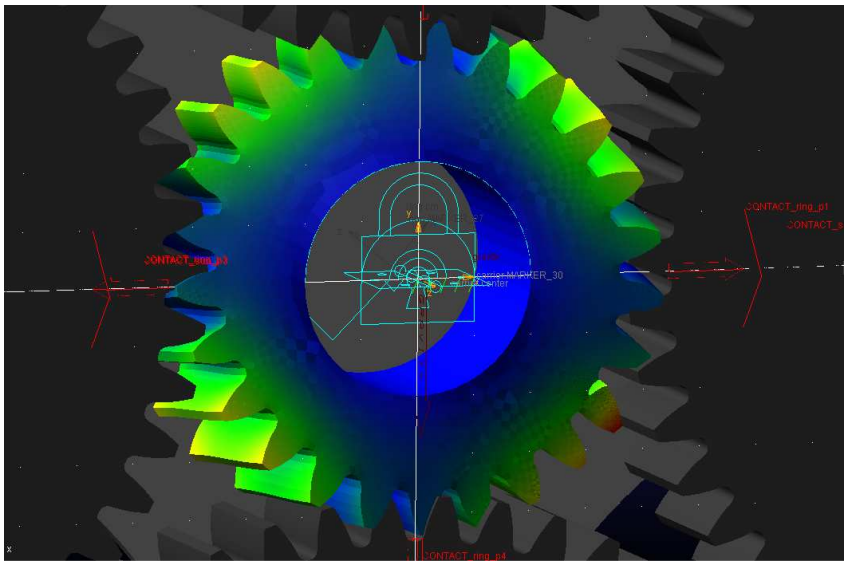

Figure 5-5: Mode of a flexible body in MSC.Adams

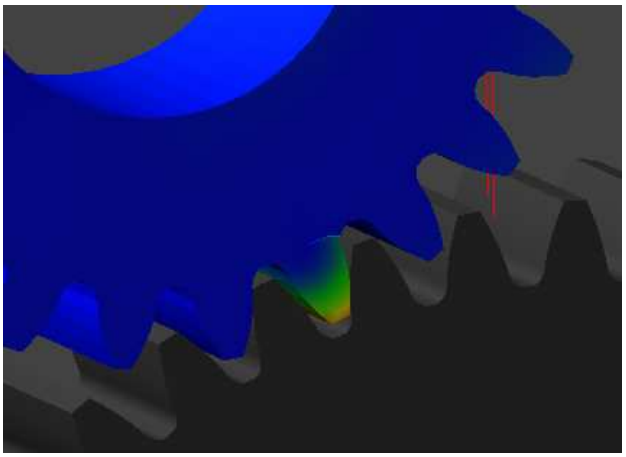

Figure 5-6: Deformed tooth during simulation

5.2 Theory of Flexible Bodies

To simulate the behavior of flexible bodies, all flexible parts need to have a finite element model structure. Due to this structure the DOF which are infinite becomes finite. However, due to more than ten thousands of nodes, the number of DOF is still very large.

Each part has its own local reference frame (coordinate system) that is defined by a position vector to the global reference frame. ADMAS FLEX_BODY's considers only small, linear body deformations at the local reference frame of the flexible body. This small linear deformations can be approximated as a combination (superposition) of a number of shape vectors. Shape vectors can be determined with a modal frequency analysis. This proceeding is called modal superposition.

5.2.1 Modal analysis

The modal analysis done by an FEM Software includes a numerical characterization of the dynamic behavior of vibrating systems using their natural vibration parameters (modal parameters): natural frequency, mode shape, modal mass and modal damping. The vibration behavior in a given operational condition is, however, detected by the vibration analysis operation.

The first step for flexible bodies is to find the natural frequencies and the natural modes of an undamped system. In the case of a free vibration no external forces are present. The equation of motion of an undamped system, written in symbolic form is

$$\underline{M}\ddot{\vec{u}} + \underline{K}\vec{u} = 0 \tag{5-1}$$

where $\underline{M}$ is the mass matrix and $\underline{K}$ is the stiffness matrix in N x N size. N is the number of physical displacement coordinates. The mass matrix $\underline{M}$ is based on the nodal masses defined through the nodes of the mesh of the part. The stiffness matrix $\underline{K}$ is also defined by the mesh of the part.

Considering a harmonic motion the displacement is,

$$u(t) = u_o * \cos(\omega t) \tag{5-2}$$

and the acceleration is,

$$\ddot{u}(t) = -\omega^2 * u_o * \cos(\omega t) \tag{5-3}$$

The algebraic eigenvalue problem for the Nth-order is,

$$\left[\underline{K} - \omega^2 * \underline{M}\right] * \overrightarrow{u_o} = 0 \tag{5-4}$$

it is necessary for a nontrivial solution to,

$$det\left(\underline{K} - \omega^2 * \underline{M}\right) = 0 \tag{5-5}$$

This equation is also called characteristic equation and solves the eigenvalue problem. The determinant is a polynomial equation of the degree N in ω^2, which are the **natural frequencies**:

$$0 \leq \omega_1^2 \leq \omega_2^2 \leq \cdots \leq \omega_r^2 \leq \cdots \leq \omega_N^2 \tag{5-6}$$

Insert each ω^2 back in to equation 5-4 to obtain N numbers of systems of equations. Solving theses equations will lead to the mode shape vector $\overrightarrow{u_o}$. For each eigenvalue ω_r^2 a corresponding natural **modes shape $\overrightarrow{u_o}$** exists[41].

$$\overrightarrow{u_o} = \begin{Bmatrix} u_{o_1} \\ u_{o_2} \\ \vdots \\ u_{o_N} \end{Bmatrix} \tag{5-7}$$

[41] Reference [31, p. 283]

The mode shape is determined uniquely, but not the modes amplitude. Scaling the natural mode is a process called normalizing so that each of its elements has a unique value. The resulting modal vectors are called normal modes Φ. All the normal modes are then collected in the modal matrix[42],

$$\underline{\Phi} = \left[\overrightarrow{\Phi_1} \quad \overrightarrow{\Phi_2} \quad \ldots \quad \overrightarrow{\Phi_N} \right] \tag{5-8}$$

5.2.2 Modal Superposition

The principle of modal superposition is that the very large number of nodal DOF can be represented with considerably less modal DOF. Therefore the linear deformation of the nodes u is the sum of the considered mode shapes (shape vectors $\vec{\phi}$ multiplied with their amplitudes q).

$$\underline{u} = \sum_{i=1}^{M} \overrightarrow{\phi_i} * q_i \tag{5-9}$$

The linear deformation u can also be represented in matrix form which is necessary for the computation of the simulation. Hence, the modal matrix $\underline{\Phi}$ (equation 5-8) contains the shape vectors $\vec{\phi}$ in its columns. Multiplying this matrix with the vector $\vec{q}$ that has the amplitudes of the mode shapes in its rows, results in a larger set of physical coordinates in the linear deformation matrix $\underline{u}$.

5.2.3 Modal flexibility in Adams

This section shows how modal superposition is applied for the kinematics of the part. The location of a node P, defined by the vector $\overrightarrow{r_P}$, on a flexible body B, is the sum of three vectors,

$$\overrightarrow{r_P} = \vec{x} + \overrightarrow{s_p} + \overrightarrow{u_P} \tag{5-10}$$

as also shown in **Figure 5-7**. Where $\vec{x}$ is the position vector from the ground origin to the origin of the local body reference frame B, $\overrightarrow{s_p}$ is the position vector from the local body reference frame of B to the undeformed position of point P (this is a constant) and $\overrightarrow{u_P}$ is the translational deformation

[42] Reference [31, p. 326]

vector of point P, the position vector from the point's undeformed position to its deformed position.

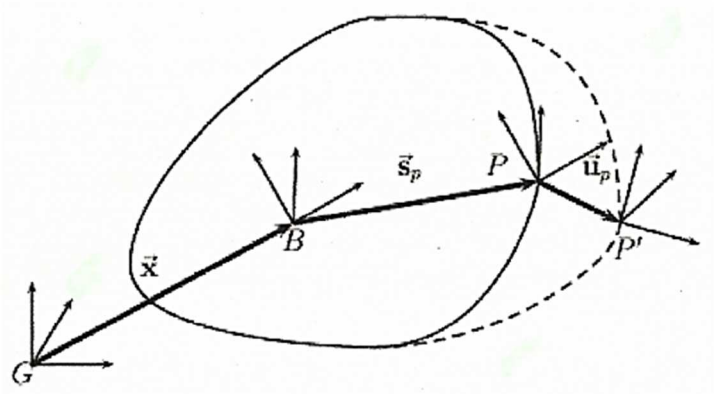

Figure 5-7: The position vector to a deformed point P' on a flexible body relative to a local body reference frame B and ground G
(Reference [11, p. Flexible Marker Kinematics])

The translational deformation vector $\overrightarrow{u_P}$ is a modal superposition (see equation 5-9) and can also be written in matrix form,

$$\underline{u_p} = \underline{\Phi_P} * q \tag{5-11}$$

$\underline{\Phi_P}$ is a 3xM matrix where M is the number of mode shapes. The 3 rows are for the corresponding translational DOF of node P. A similar approach is used for the orientation of the node P. The angles that are used to describe the orientation are the difference of the deformed node and the undeformed. This is obtained by the corresponding rotational DOF of node P.

At this point of the derivation the flexible body generalized coordinates are introduced as,

$$\xi = \begin{Bmatrix} x \\ y \\ z \\ \psi \\ \theta \\ \phi \\ q_i (i = 1 \dots M) \end{Bmatrix} \tag{5-12}$$

with the generalized coordinates (x, y and z), the Euler angles (ψ, θ and ϕ) of the flexible body and the modal coordinates ($q_i (i = 1 \dots M)$).

To apply the influence of mode shapes to the kinematic of the system, the governing equations for a flexible body, derived from Lagrange's equation, is used as an approach,

$$\frac{d}{dt}\left(\frac{\partial L}{\partial \dot{\xi}}\right) - \frac{\partial L}{\partial \xi} + \frac{\partial F}{\partial \xi} + \left[\frac{\partial \Psi}{\partial \xi}\right]^T * \lambda = Q \qquad \text{(5-13)}^{43}$$

L : Lagrangian, $L = T - V$

F : Energy dissipation function

Ψ : Algebraic constraint equations

λ : Lagrange multipliers for the constraints

ξ : Flexible body generalized coordinates

Where the kinetic energy T is, considering the modal mass m_p, translational velocity v and rotational velocity ω,

$$T \approx \frac{1}{2}\sum_p \left[m_p * {v^T}_p * v_p + {}^G\omega_p^{BT} * I_p * {}^G\omega_P^B\right] \qquad \text{(5-14)}$$

the potential energy V is, considering the density ρ, the gravitational acceleration vector $\vec{g}$ and the location of node P, $\overrightarrow{r_P}$,

$$V = \int_v \rho \overrightarrow{r_p} * \vec{g}\, dv \qquad \text{(5-15)}$$

With this approach the equation of motion can be derived. The equations of motion are used to describe the dynamic behavior of a multi body system,

$$M\ddot{\xi} + \dot{M}\xi - \frac{1}{2}\left[\frac{\partial \mathrm{M}}{\partial \xi}\xi\right]^T \xi + D\dot{\xi} + f_g + K\xi + \left[\frac{\partial \Psi}{\partial \xi}\right]^T * \lambda = Q \qquad \text{(5-16)}^{44}$$

M : Flexible body mass matrix

D : Modal damping matrix

K : Generalized stiffness matrix

f_g : Generalized gravitational

Q : Generalized applied forces

---

[43] Reference [11, p. Flexible Body Equations of Motions]

[44] Reference [11, p. Flexible Body Equations of Motions]

This full equation of motion considers all aspects of the MBD simulation, including the Coriolis and centrifugal effects as well as the influence due to gravitational acceleration and constrains of the node kinematics. A full presentation and derivation of the complete equation of motion is beyond the scope of this thesis. To show how the flexible body structure influences the equations of motion and the dynamic behavior of the system, a simplified equation of motion (from equation 5-1) will be considered for further presentations[45].

$$M\ddot{\xi} + K\xi = Q \tag{5-17}$$

Hence, based on equation (5-14) with the modal mass m_p, neglecting of I_p, substituting for translational velocity v and rotational velocity ω, the kinetic energy is after simplification,

$$T = \frac{1}{2} * \xi^T * M(\xi) * \xi \tag{5-18}$$[46]

The flexible body mass matrix[47] is,

$$M(\xi) = \begin{bmatrix} M_{tt} & M_{tr} & M_{tm} \\ M_{tr} & M_{rr} & M_{rm} \\ M_{tm} & M_{rm} & mm \end{bmatrix} \tag{5-19}$$

(The subscripts t,r and m denote translational, rotational, and modal DOF respectively)

where,

$M_{tt} = I^1 * \mathbf{I}$

$M_{tr} = -A * \left[I^2 + I_j^3 q_j\right] * B$

$M_{tm} = A * I^3$

$M_{rr} = B^T * \left[I^7 - \left[I_j^5 + I_j^{5T}\right] q_j - I_j^9 q_i q_j\right] * B$

$M_{rm} = B^T * \left[I^4 + I_j^5 q_j\right]$

$M_{mm} = I^6$

$I^1 = \sum_{p=1}^{N} m_p$	$I^4 = \sum_{p=1}^{N} m_p * s_p * \Phi_p$	$I^7 = \sum_{p=1}^{N} m_p * {s_p}^T * s_p$

[45] Neglected values: Coriolis and centrifugal effects, modal damping, gravitational force, node constraints.

[46] Reference [11, p. Flexible Body Equations of Motions]

[47] Reference [11, p. Flexible Body Equations of Motions]

$I^2 = \sum_{p=1}^{N} m_p * s_p$	$I_j^5 = \sum_{p=1}^{N} m_p * \phi_{pj} * \Phi_p$	$I_j^8 = \sum_{p=1}^{N} m_p * s_p * \phi_{pj}$
$I_j^3 = \sum_{p=1}^{N} m_p * \Phi_p$	$I^6 = \sum_{p=1}^{N} m_p * {\Phi_p}^T * \Phi_p$	$I_{jk}^5 = \sum_{p=1}^{N} m_p * \phi_{pj} * \Phi_{pk}$

The generalized applied forces Q consist of a generalized translational force Q_T, a generalized torque Q_R and a generalized modal force Q_M,

$$Q = \begin{bmatrix} Q_T \\ Q_R \\ Q_M \end{bmatrix} \tag{5-20}$$

The generalized translational force $Q_T\ is$,

$$Q_T = {}^G A^K * F_K \tag{5-21}$$

The generalized torque Q_R is,

$$Q_T = \left[{}^G A^K * B \right]^T * T_{tot} \tag{5-22}$$

with

$$T_{tot} = {}^G A^K * T_K + p * {}^G A^K * F_K \tag{5-23}$$

The generalized modal force Q_M is projecting the load on the mode shapes,

$$Q_M = \Phi_p^T * F_I + {\Phi_p^*}^T * T_I \tag{5-24}$$

Where Φ_p and Φ_p^* are the slices of the modal matrix corresponding to the translational and angular DOF at Point P.

$$F_I = {}^G {A^B}^T * {}^G A^K * F_K \tag{5-25}$$

$$T_I = {}^G {A^B}^T * {}^G A^K * T_K \tag{5-26}$$

5.2.4 Verification of Applied Flexible Body Theory

To verify the flexible body theory, simple geometry was first considered (see **Figure 5-8**). Therefore the flexible behavior of the body can be calculated by reliable and trusted standard calculations. Additionally a Finite Elements Method (FEM) analysis with Abaqus was performed. The flexible behavior in MSC.Adams has to match those two previous calculations. For a structural beam (length l=150 mm, width b=40 mm; height h=20 mm), which is fixed at one end and a load applied at the other end, the deflection of the unsupported end is defined as,

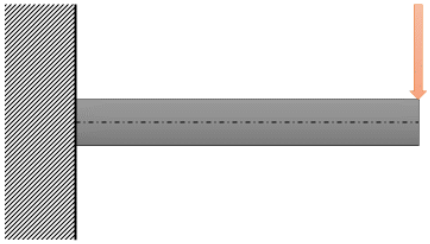

Figure 5-8: Simple structural beam geometry

$$u = \frac{F * l^3}{3 * E * I} \tag{5-27}$$

where F is the applied force , E is the Young's modulus, and I is the second moment of inertia which is defined as,

$$I = \frac{b * h^3}{12} \tag{5-28}$$

Therefore the hand calculation shows a deflection of 1.019E-04 m and the FEM calculation shows a deflection of 1.032E-04 m. With the MBD analysis, the deflection is 1.027E-04 m which shows that the MBD Simulation is matching the standard procedures to calculate deflection (see **Table 5-2**).

Table 5-2: Deflection calculation comparison of different calculation methods

Hand calculations	$$u = \frac{500\ N * (0.15\ m)^3}{3 * 2.07E11\ \frac{N}{m^2} * \frac{0.04\ m * (0.02\ m)^3}{12}}$$	Deflection **1.019E-04 m**
FEM calculation in Abaqus	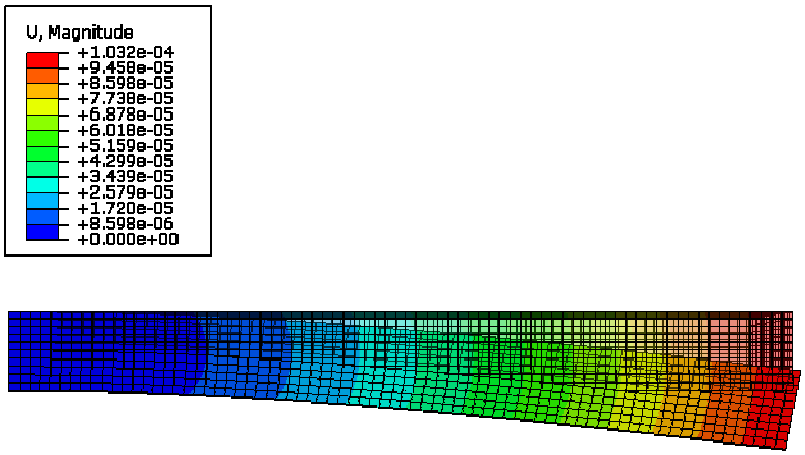	Deflection **1.032E-04 m**
MSC.Adams analysis	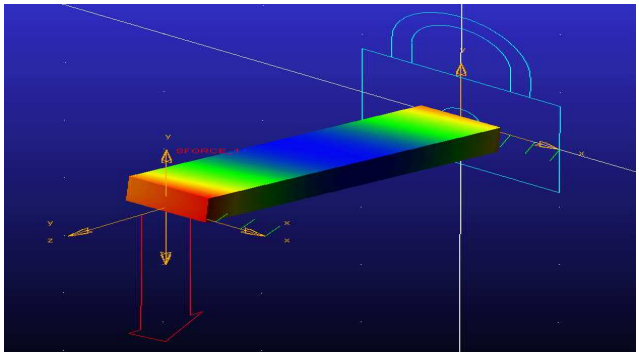	Deflection **1.027E-04 m**

For complex parts a hand calculation is not possible. **Table 5-3** shows the FEM calculation compared to the MBD results for the deflection of a tooth.

Table 5-3: Comparison of the deflection of a tooth for different calculation methods

FEM calculation in Abaqus	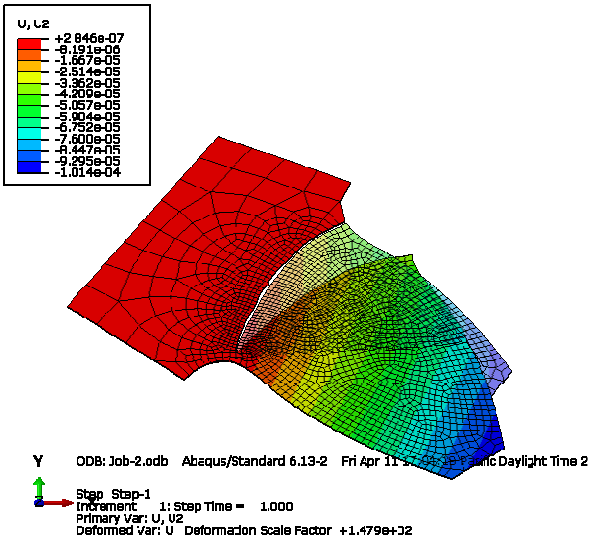	Deflection **1.014E-04 m**
MSC.Adams analysis	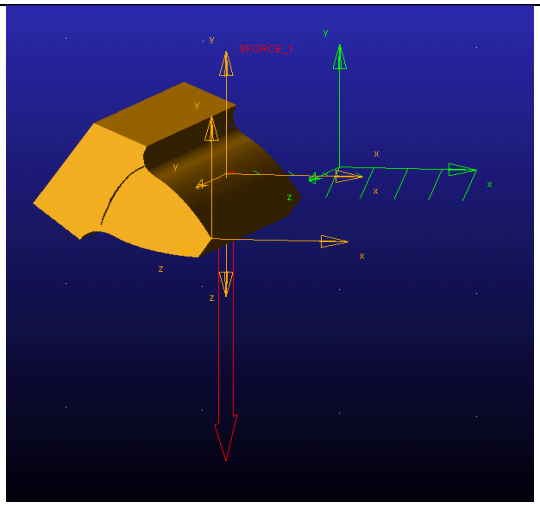	Deflection **1.02E-04 m**

This calculation shows a deflection of 1.014E-04 m for FEM and 1.02E-04 m for MBD simulation. This again proves that even for complex parts, the flexible bodies in MSC.ADAMS have a right behavior. The deflection is matching with the FEM calculation of Abaqus.

5.3 Simulation Step Size

The step size has to be as large possible and as small as necessary. That is because of the very long simulation times that can occur. The step size hast be smaller for higher forces, which leads to an “intense” contact point, and for fast moving parts. The step size can be figured out by trail and error (starting the simulation and pausing it to see if the behavior of the system is as expected).

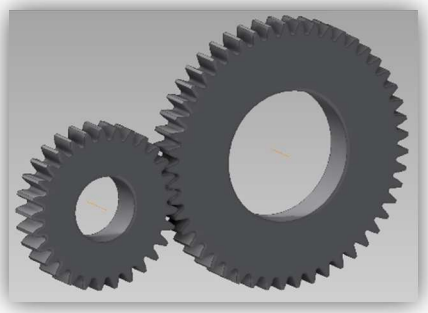

Figure 5-9: Simulated gear

Figure 5-9 displays a gear that has been used for further simulations. It is recommended to start with a simple model to get a rough value range of the necessary parameters for future more complex systems.

Figure 5-10 shows the contact force of a gear tooth with a step size of a tens of a second (0.1 seconds). Due to the constant motion of the sun gear and the very high torque of the planet gear, the teeth between the two gears are expected to be in constant contact. As the figure shows there are many drops in the contact force as well as many unexpected peaks. This occurs because of the high simulation steps in the model. The simulation time is a discrete signal. Therefore a contact between two parts means that one part penetrates the other. This penetration should be very small and a maximum allowable penetration depth (0.01 mm) is defined in the model. This penetration generates a penalty force which defines the contact force. If the step size is too large, one tooth of the gear penetrates the other tooth too deeply and as a result of that there will be a very high penalty force. This behavior is shown in Figure 5-10.

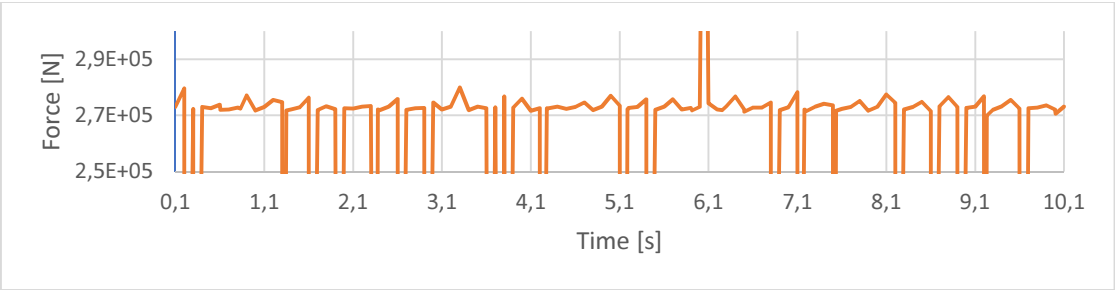

Figure 5-10: Contact force of gear teeth with step size of 0.1 seconds

With a step size two times finer (0.05 second) the number of drops and peaks can be reduced as seen in **Figure 5-11**. Additionally the value of the drops and peaks itself are lower. But they are still present and will have influence of the on FFT analysis which will result in noise.

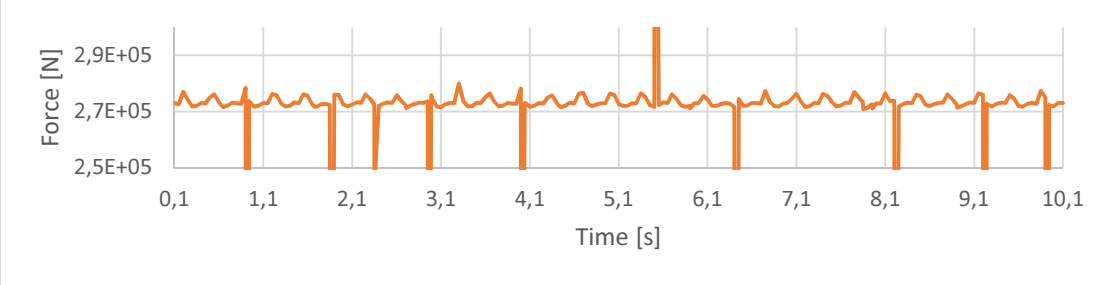

Figure 5-11: Contact force of gear teeth with step size of 0.05 seconds

Figure 5-12 shows that with a step size of 0.01 seconds the unexpected forces disappear.

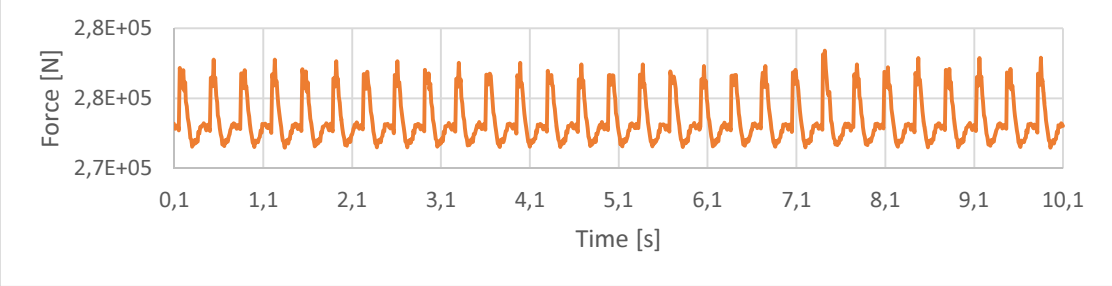

Figure 5-12: Contact force of gear teeth with step size of 0.01 seconds

Figure 5-13 shows a close view of the simulation step sizes of 0.05 and 0.01 seconds. It is visibly obvious, that the resolution of 0.01 seconds shows the actual contact force much clearer than larger steps.

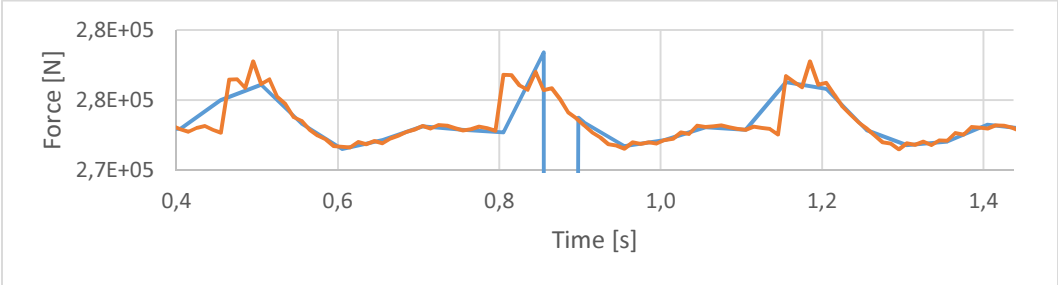

Figure 5-13: Contact force of gear teeth with step size of 0.05 and 0.01seconds

Figure 5-14 shows that the noise of the contact force can be further reduced with finer steps. However a fine step size of 0.003 will lead to a very long simulation time which is not preferred and not necessary for the aimed simulation purpose.

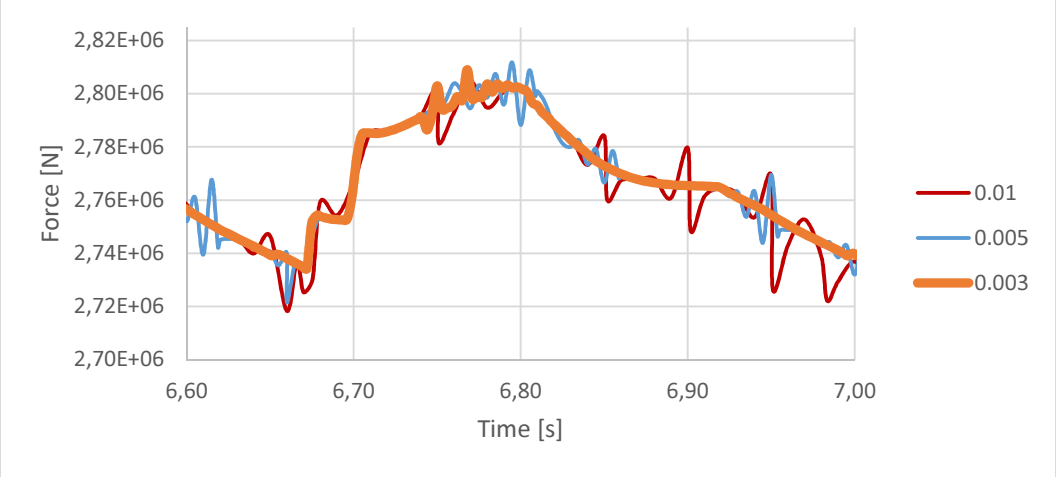

Figure 5-14: Contact force of gear teeth with step size of 0.001 seconds

5.4 Stiffness Value and Contact Forces

5.4.1 Theory to Approach Solutions of Contact Forces and Stiffness

The standard theory to approach solutions of contact forces and stiffness is the Hertz theory. However, for the contact of cylindrical bodies such as gears (**Figure 5-15**) or roller bearings, the Hertz theory is not solely sufficient to determine these parameters. In this case, the shape and size of the bodies themselves are important. In most practical analyses these calculations are difficult to perform and a lot of different approximations and assumptions have been developed over time.

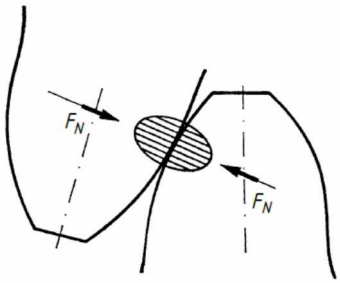

Figure 5-15: Line contact at gear contact
(Reference [9, p. 83])

For the simulation of the contact in MSC.Adams, the stiffness of the bodies is necessary to perform the calculations. The theory of K.L. Johnson, “contact of cylindrical bodies” is extended by Vink System Design & Analysis[48] will be considered as seen in **Figure 5-16**:

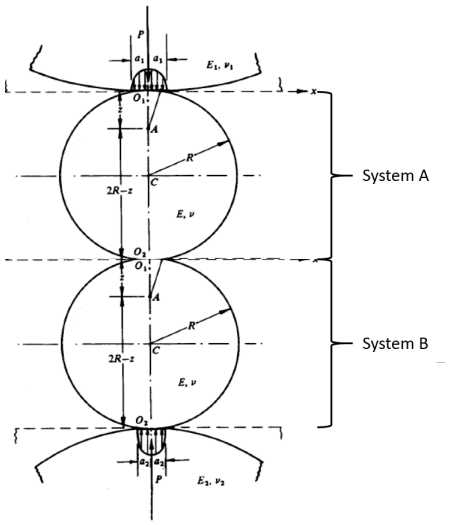

Figure 5-16: Extended approach of contact of cylindrical bodies
(Reference [12, p. 130])

To determine the stiffness of the body, the calculation is based on the stiffness k defined as,

$$k = \frac{F_N}{\sigma} = \frac{F_b}{\sigma} \tag{5-29}$$

where the normal force F_N is the tooth force F_b and σ is the displacement of the contact point. To perform the calculations with the theory of cylindrical bodies, the radius of the contact teeth has to be approximated as seen in **Figure 5-17**. Which leads to a tooth radius R_1 for the pinion and R_2 for the gear.

[48] Applied in HertzWin 2.3.1

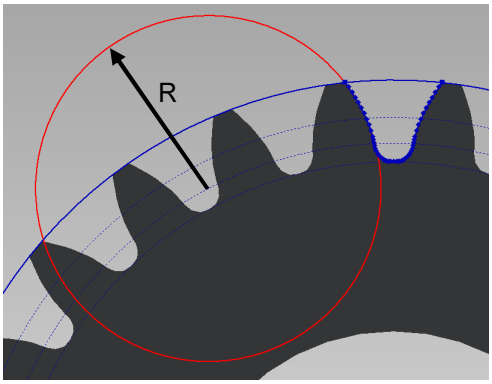

Figure 5-17: Approximation of tooth radius

The displacement of the contact point σ can be defined as,

$$\sigma = 2 * P * \frac{(1-v^2)}{\pi * E} * \left[\ln(\frac{4 * R_1}{a_1}) + \ln\left(\frac{4 * R_2}{a_2}\right) - 1\right] \quad (5\text{-}30)^{49}$$

Where the compressive load per unit axial length P can be defined with the tooth force F_b and the facewidth b of the gear as,

$$P = \frac{F_b}{b} \quad (5\text{-}31)$$

Where the semi-contact-width is given by,

$$a_{1/2}^2 = \frac{4 * P * R_{1/2}}{\pi * E^*} \quad (5\text{-}32)^{50}$$

The composite modulus E^* is given as

$$E^* = \frac{2 * E_1 * E_2}{(1-v_1^2) * E_2 + (1-v_2^2) * E_1} \quad (5\text{-}33)^{51}$$

where E_1 and E_2 are the young's modulus and $v_1$and v_2 the passion's ratio of the contact materials.

However, because of a dynamic simulation with changing tooth forces over time, the stiffness of the contact, which is defined for each contact and not for each body, has to be a rough approximation due to the previous calculations.

[49] Reference [12, p. 131]

[50] Reference [12, p. 129]

[51] Reference [9, p. 83]

For the gearbox of this analysis, the contact stiffness fluctuation due to changing parameters is roughly,

$$k = 4\ E^{06}\frac{N}{mm} \quad \dots \quad 6\ E^{06}\frac{N}{mm} \tag{5-34}$$

An analysis of the contact behavior has shown that the system behavior due to the differences is not significant and often does not have any influence at all. A noticeable difference can be seen at higher factors of 10 or 100. Therefore a stiffness value k of $5\ E^{06}\frac{N}{mm}$ has been used for the simulation.

5.4.2 Penetration Depth

The penetration depth is a value that defines at what amount of penetration the solver will use full damping. The solver uses a step function to increase the damping parameter. At zero penetration the damping parameter is zero as well. With increasing of the penetration depth of the surface into the other, the damping parameter increases too, until full damping value is reached. MSC.Adams suggests a reasonable value of 0.01mm for this parameter.

5.4.3 Damping

The damping value defines the properties of the material with which is in contact. MSC.Adams suggests a damping coefficient that is about 1% of the stiffness coefficient.

5.4.4 Force exponent

The force exponent is a parameter of the IMPACT function's spring force which has the recommended value e>1. The value itself is a material property[52]. The force exponent increases for harder materials[53].

- Very soft materials (rubbers) force exponent of e=1.1
- Soft metals (aluminum) force exponent of e=1.5
- Hard metals (steel) force exponent of e=2.2

[52] Reference [30]

[53] Reference [29, p. 28]

6 ANALYSIS OF MULTI BODY DYNAMICS SIMULATION OF WIND TURBINES

In this chapter the analysis of multi body dynamics simulation of wind turbines will be discussed. The type and shape of the simulated **tooth crack** is discussed in 6.1 as well as the **detection of cracked tooth** of in 6.3. In 6.4 the **gear mesh frequency (GMF)** is introduced which is a very important analyzing parameter. The **fast fourier transformation (FFT)** that is applied to analyze the vibrational behavior is presented in 6.5. The **results of the analyses** is discussed in 6.6 as well as the handling of the results in 6.7 to generate an **operating number** to compare vibrational behavior.

6.1 The Simulated System

6.1.1 Overview

For this paper a Nordex N90/2300 wind turbine was used to simulate the vibrational behavior. Hence, no technical drawings or other information were given by the manufacturer. Therefore, the gearbox is designed according to the design guide from chapter 4.6 on page 29, based on the specification sheet of the Nordex N90/2300. The used simulation parts are therefore not exactly the same, but are very close to the original gearbox with the same specifications. The simulation hardware is for that reason very close to an applied

Figure 6-1: Nordex wind turbine (Reference [1])

industrial application and reflects applications in reality. **Figure 6-2** shows the gearbox of the Nordex N90/2300 in the nacelle of the wind turbine.

Figure 6-2: Inside nacelle of the Nordex wind turbine
(Reference [1])

6.1.2 The Gearbox

The used gearbox has following parameters as seen in **Table 6-1**:

Table 6-1: Parameter of the gearbox for N90/2300 [3, p. 7]

Type	**Three stage planetary / spur gear system**
Gear ratio	1 : 77.44
Operation input speed	15.5 rpm (1.62 rad/s or 93 deg/s)

The three stage gearbox has 2 planetary gear stages and one spur gear stage. Table 6-2 shows the parameters that have been used for the gear design.

Table 6-2: Parameter of the 1st and 2nd stage

Type	1st Stage	2nd Stage
# Teeth's Sun	25	32
# Teeth's Planet	47	145
# Teeth's Ring	119	322
# of planets	4	3
Pitch Diameter Sun	400 mm	192 mm
Pitch Diameter Planet	752 mm	870 mm
Pitch Diameter Ring	1904 mm	1932 mm
Center Distance	576 mm	531 mm
Gear Ratio	5,76	11,06
Module	16 mm	6 mm
Backlash Normal Backlash j_n:	1.65 mm	0.65
Tooth width	150 mm	150 mm
Thickness of the Ring Rim	100 mm	100 mm
Bottom Clearance	4.8 mm	1.8 mm
Pressure Angle	20°	20°
Material	18CrNiMo7-6 AISI 4820 UNS G48200	18CrNiMo7-6 AISI 4820 UNS G48200

Figure 6-3 shows the first stage of the wind turbine gear box.

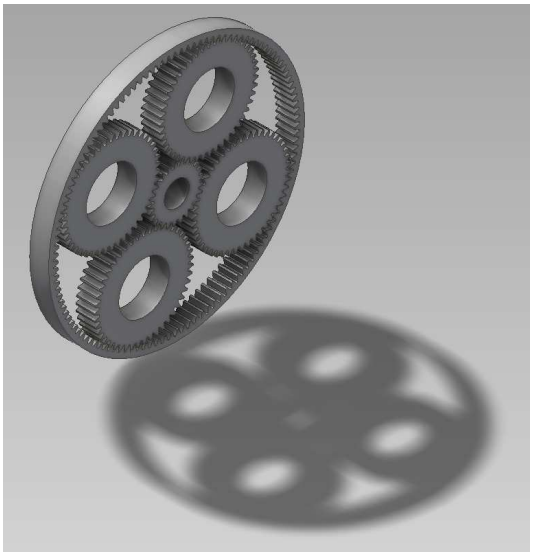

Figure 6-3: Gears of 1st stage

6.1.3 Input Force

Figure 6-4 shows the input values of a Nordex N90/2300 wind turbine which is used in the MBD Simulation. Please see chapter 2.3 on page 14 to find the derivation of this graph.

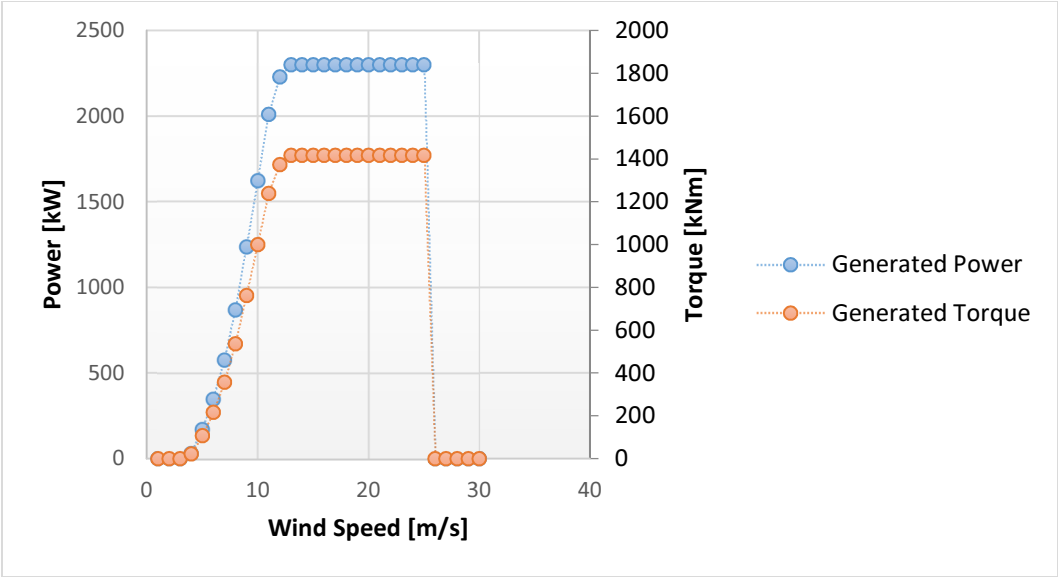

Figure 6-4: Generated power and torque

6.1.4 Relative speeds

Relative speeds based on equations of chapter 4.10 on page 38. These values occur with maximum torque at the rotor at wind speeds of 14-25 m/s.

Table 6-3: Relative speeds of 1st stage

GEAR	RPM
CARRIER	15.5
PLANET JOINT	-39.24
PLANET ANGULAR VELOCITY CM	-23.74
SUN	89.28

6.1.5 The Generator

The blue curves in **Figure 6-5** shows the power in dependency of the rotor speed. Therefore the maximum power output at certain wind speeds is dependent on the rotor speed. The N90/2300 is equipped with two asynchronous generators as shown in the diagram. The power output is therefore defined by the current wind speed and the operational rotor speed.

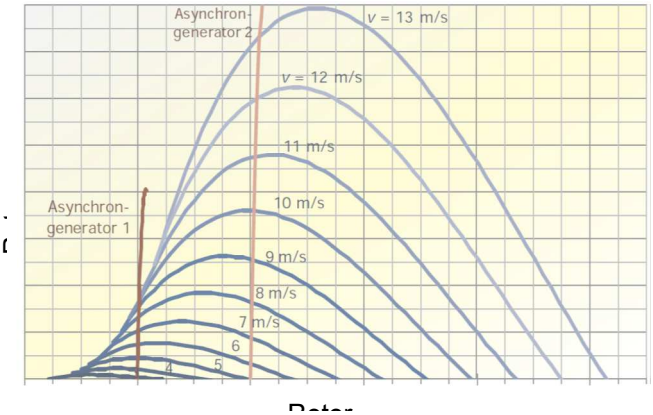

Figure 6-5: Operational points of a wind turbine with two asynchronous generators of different speeds
(Reference [2, p. 303])

It can be assumed that that the generator and the breakage system would regulate the resulting rotor speed relative constant. The gearbox system will be regulated by a simple function that holds the operation output speed at 1200 rpm. With the given gear ratio of 77.44 the input speed is 15.5 rpm.

6.2 Damaged tooth, cracked sun gear tooth

As discussed in chapter 3 on page 15, several gear failure modes apply to wind turbine gears. However, in this thesis tooth breakage is the content of the analysis. A tooth of the sun gear of

stage one has been cracked. Therefore the sun gear is simulated as a flexible body based on the FEA results. To simulate different stages of the failure, different sizes of cracks have been considered. **Figure 6-6** shows the different cracks of the sun gear. To define the length of a crack independent of the gear size, the crack length is given as a percentage of the total length.

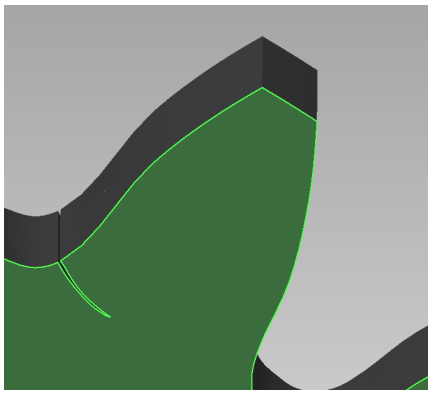

Short crack, 33.5%

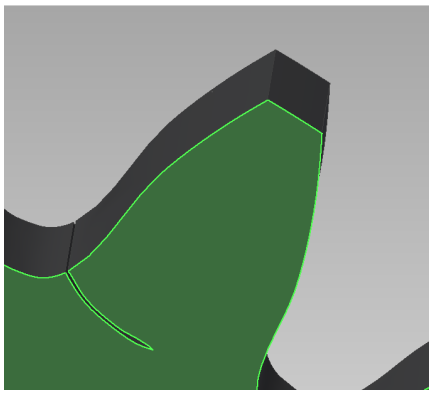

Middle crack, 51.6%

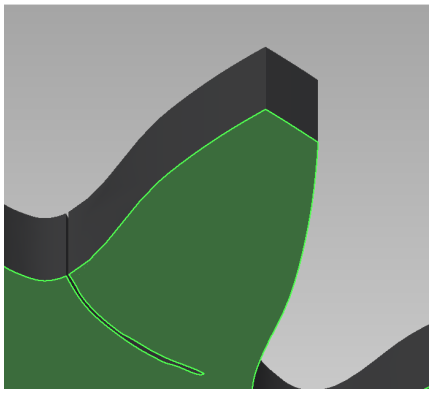

Long crack, 77,2%

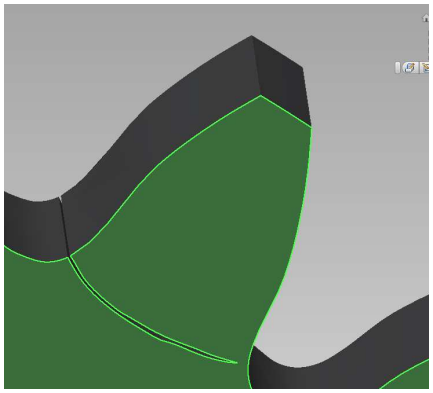

Extra-long crack, 94.7%

Figure 6-6: Tooth Root Cracks on the Sun Gear

6.3 Tooth root damage detection

In the simulation the contact force can be analyzed to detect if a tooth is cracked. **Figure 6-7** shows that there is an increase of force where the cracked tooth is in contact. The discrepancy is getting lower with time until it reaches the normal (like a perfect gear) condition.

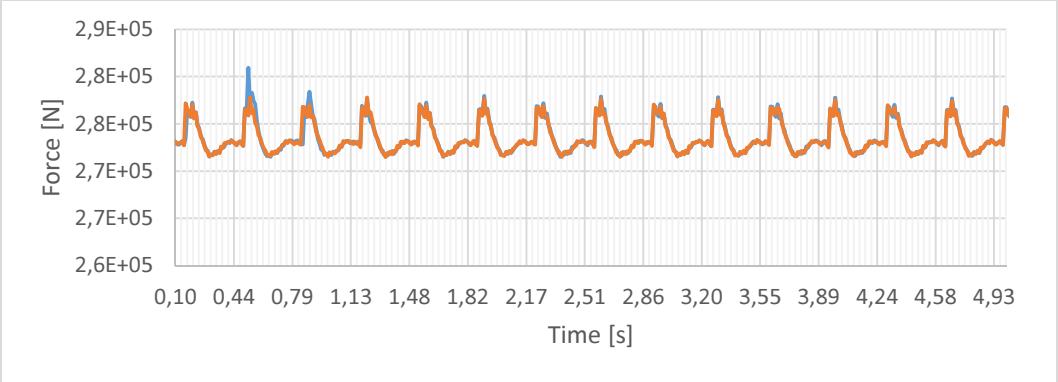

Figure 6-7: Contact force of perfect gear vs. tooth root breakage, step size of 0.01

The influence of a cracked gear is shown in the close view in **Figure 6-8**. The cracked gear is in contact for 0.7 seconds. The contact starts at 0.5 seconds. There are always two teeth in contact. The highest influence of the cracked tooth is when it starts the contact. When the next perfect tooth joins the contact, the influence of the cracked tooth is lower but still visible. As soon as the cracked tooth is not in contact the force shows normal behavior. This shows that due the simulation, the cracked tooth can be detected.

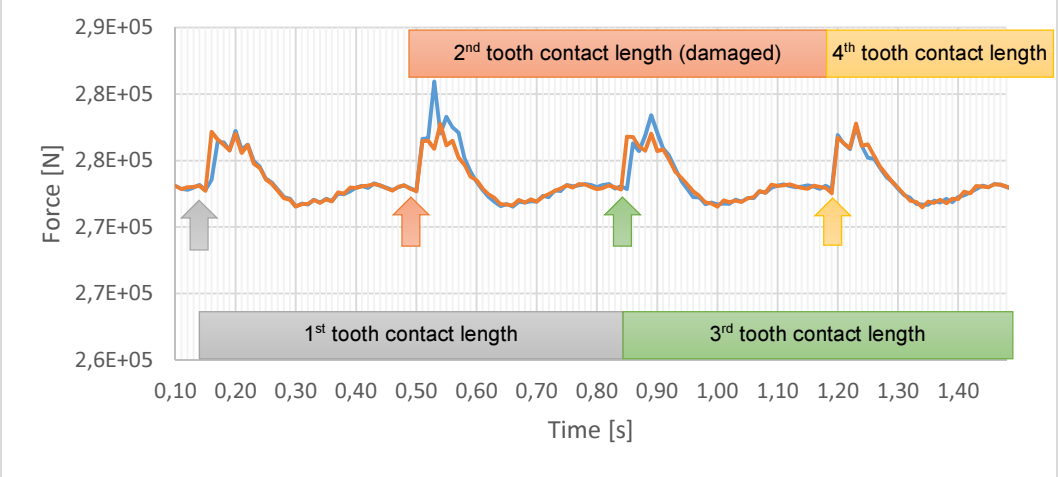

Figure 6-8: Contact force of perfect gear vs. tooth root breakage, step size of 0.01

However, in a real world application it is not possible to measure the force at the contact surface. This can only be analyzed with a simulation on a computer. To represent the forces of a real gear, the vibrational behavior can be measured with accelerometers. This vibration is related to

contact forces inside of the gear box and can reflect these forces. This conclusion is proven with several other thesis projects at the Cal Poly Engineering department[54].

6.4 Gear Mesh Frequency (GMF)

The gear mesh frequency (GMF) is an important parameter for further analysis of the simulation. It shows at what frequency one tooth of the gear is going to mesh with another. **Figure 6-9** shows the time that passes from one tooth contact to the next. With that time known, the contact frequency or gear mesh frequency can be calculated.

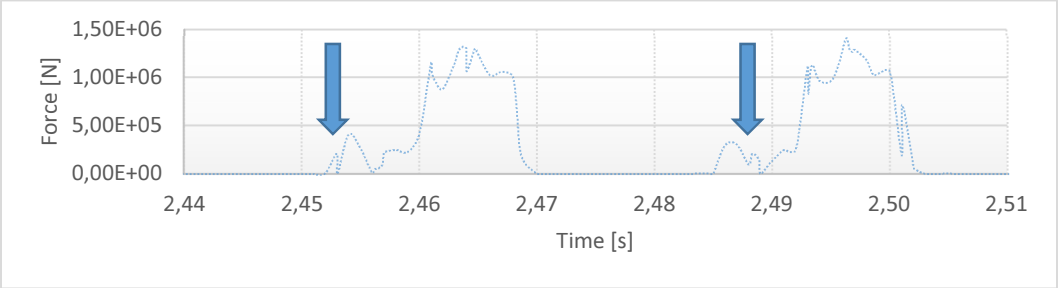

Figure 6-9: Time until new tooth contact

The following equation shows the calculation for the gear mesh frequency for a given RPM and number of teeth

$$GMF = \frac{z * RPM}{60} \tag{6-1}$$

For the gearbox of the N90-2300 in stage one where the tooth is cracked the GMF is 30.738 (Ring-Planet / Sun-Planet). This value has an important role for the vibration analysis in 6.6 on page 72. This is because the expected frequency of the vibration is expected at this specific value (and at integer multiplies of it). All other frequencies that appear will be noise. Therefore, a change in the vibrational behavior due to a cracked tooth would lead to noise and may be detected.

[54] „Vibration-Based Health Monitoring of Multiple-Stage Gear Train and Differential Planetary Transmission Involving Teeth Damage and Backlash Nonlinearity“ from Andrew Patrick Sommer in September 2011 and “CAE Methods on Vibration-based Health Monitoring of Power Transmission Systems” from Brian Fang in December 2013

6.5 Fast Fourier Transform (FFT)

To detect the error of the gear, the vibration data can be recorded with attached accelerometers on the housing of a gear. This data can be analyzed with the Fast Fourier Transform (FFT). The FFT is a different way to look at the measured contact forces of the gear.

The measured contact force is a curve of **force over time**. The FFT displays the same signal in **force over frequency**.

The French mathematician and physicist Jean-Baptiste Joseph Fourier (1768–1830) describes that a periodic function or signal can be decomposed into the sum of a set of simple sine and cosine functions.

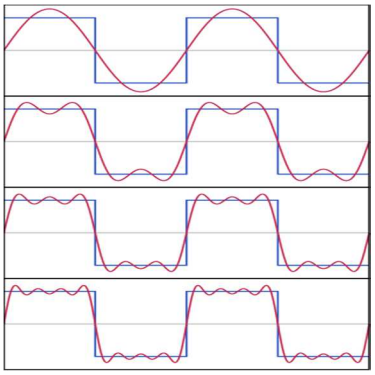

Figure 6-10: Decomposing a function (Wikipedia)

$$f(x) = \frac{a_0}{2} + \sum_{n=1}^{\infty} (a_n \cos(n\omega t) + b_n \sin(n\omega t))$$

A rectangular function as seen in **Figure 6-10** can be approximately described as a set (sum) of sine functions. Therefore the FFT shows the components of the original signal. To represent the original curve accurately, the number of added sine curves can be infinite. However, for computational calculations the number of used functions are as low as necessary.

Figure 6-11 shows one period (2π seconds) of a curve of a force time function.

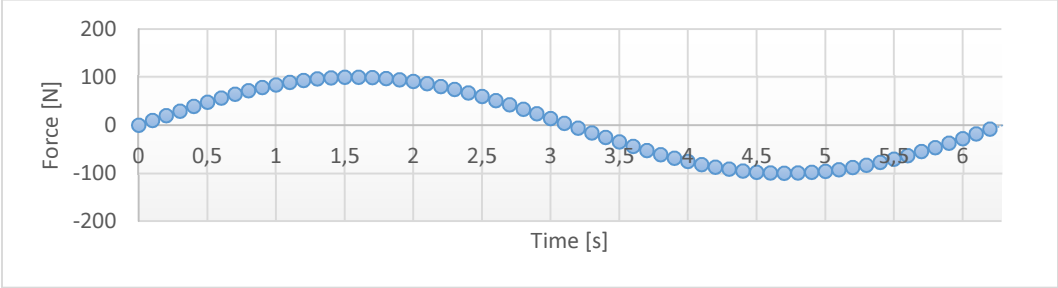

Figure 6-11: Sine function 100N*sin(time)

The FFT shows with which sine curves the original signal can be approximated. As in **Figure 6-11**, the original signal is a sine curve [100N*sin(time)], therefor it can be represented with just one sine curve of the same function. The frequency f of this sine curve is 0.16Hz,

$$f = \frac{1}{t} = \frac{1}{2\pi\ s} = 0.16\ Hz \tag{6-2}$$

The FFT shows the same signal in a force frequency diagram Therefore **Figure 6-12** shows one peak at exactly that frequency.

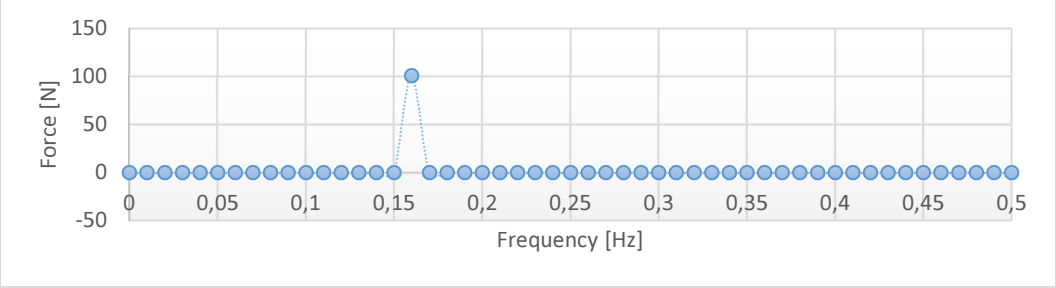

Figure 6-12: FFT for a simple sine curve

In reality, there are practically no signals that can be represented with just one sine function. The complex orange function in **Figure 6-13** can be approximated by three sine functions with different amplitudes and period times. The red curve is the basis function and the other two functions are functions with higher frequencies. Therefore the FFT shows for each sine curve a peak at each frequency which is defined by the period length.

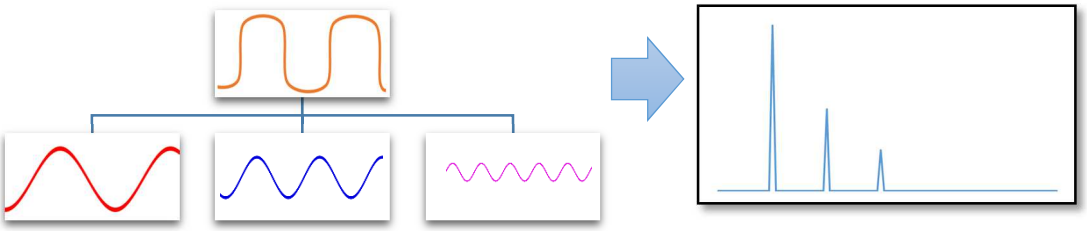

Figure 6-13: Different components of a signal

According to the Fourier series of Jean-Baptiste Joseph Fourier, the sine curves with higher frequencies (shorter periods) can only be frequencies with integer multiplies of the basis sine function. Other peaks at different frequencies are noise/ non-periodical behavior of the original signal. Gears have a periodical contact force at a specific frequency which is defined by the rotational speed of the gear and the number of teeth, see Gear Mesh Frequency (GMF) at chapter 6.1 on page 62. **Figure 6-14** shows a periodical contact force of a gear tooth and its resulting FFT.

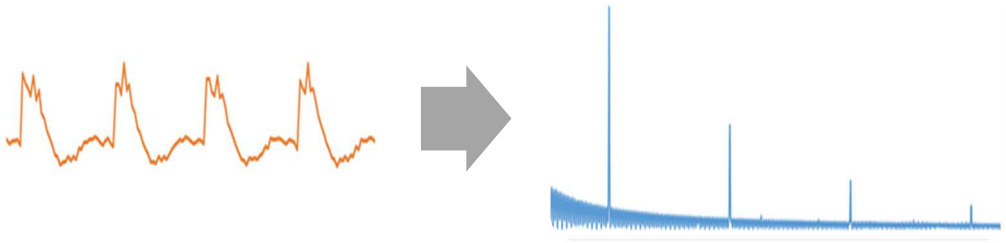

Figure 6-14: FFT of a periodical tooth contact force

Because not every contact has exactly the same force progression, noise that is shown between the peaks is expected.

6.6 Vibration Results Analysis

In this section the simulation results are shown as well as the analysis. In order to generate/calculate these results, a lot of simulations have to be done in order to eliminate all errors and choose the correct simulation parameters (See appendix B).

Figure 6-15 shows the final results of the vibration based planetary gear analysis and damage detection of the Nordex N90/2300 gear box. It is a FFT of the contact force of the cracked sun gear and the planet gears (4 planets) in stage one. This FFT is being compared with the FFT of the perfect gear. As expected, there are peaks at the gear mesh frequency (GMF) and at integer multiplies of it. For an ideal periodical signal input. the FFT should show no amplitude in the section between the GMF peaks. Therefore the force has asymmetric components. For a damaged tooth theses non-periodic components should be noticeably higher.

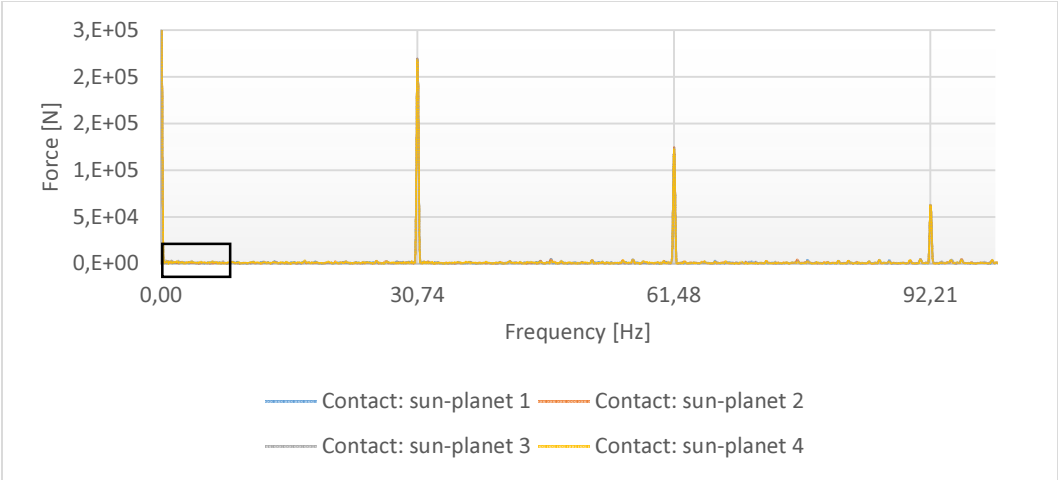

Figure 6-15: FFT of the contact force at the sun gear stage 1

Figure 6-16 shows the same data zoomed in to the frequency range of 8 to 12 Hz (black frame in Figure 6-15). This section of the FFT is the noise that occurs during the simulation. The different contact forces of the planets can now be distinguished. The forces show all the same behavior and do not differ from each other in a noticeable magnitude.

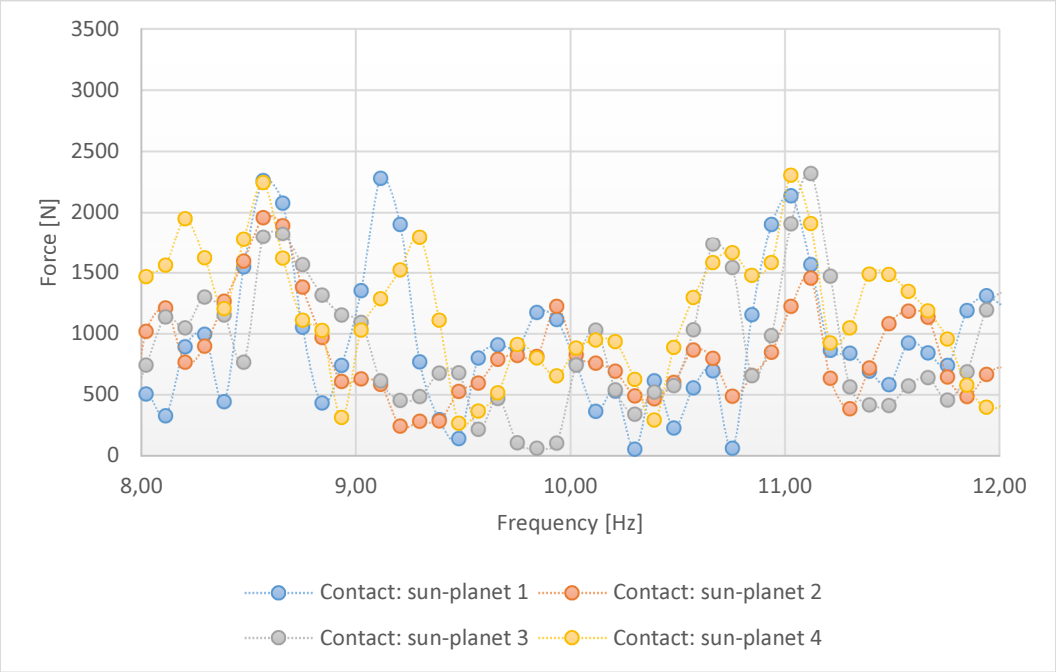

Figure 6-16: Zoom of the noise of the perfect gear

To see if there are differences in the forces with a perfect gear, the data of the cracked gear is compared with the data of a perfect one. **Figure 6-17** shows the comparison of the contact force of the second planet and the sun gear. The blue curve is the perfect gear and the red curve is the cracked gear. As seen, the curve for the cracked tooth is higher in magnitude and has bigger differences in maximum and minimum points. This higher amount of noise of the red curve indicates more non-periodic forces which occur due to the cracked tooth.

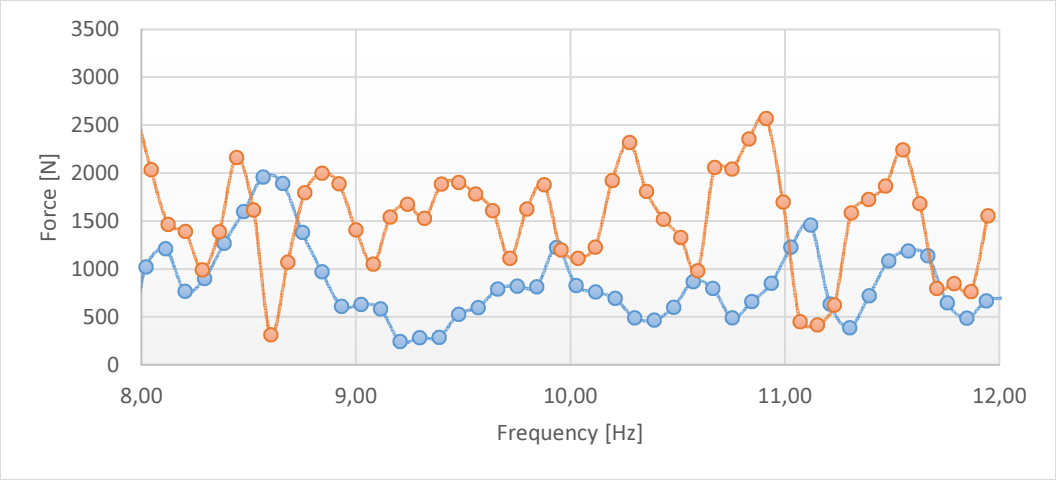

Figure 6-17: Comparison of the Cracked and Perfect Gear

This comparison proves that the FFT of the contact force of a cracked gear set shows a different vibrational behavior. Further study of the data has additionally shown that this behavior is observed at most gear contacts in the system.

6.7 Operating Numbers

To compare the FFT results of the vibration analysis it is suitable to specify a value that shows if the gearbox has issues. Hence, an operating number has been defined. This number shows the standard deviation of the noise between the GMFs of the system:

$$\sigma = \sqrt{\frac{1}{N-1} * \sum_{i=1}^{N} (x_i - \mu)^2} \quad where \quad \mu = \frac{1}{N} * \sum_{i=1}^{N} x_i \qquad (6\text{-}3)^{55}$$

In order to get just the noise of the vibration, the GMF peaks will not be considered for the standard deviation calculation. For analysis purposes the frequency range called 1st and 2nd block have been defined as shown in **Figure 6-18**.

[55] Reference [40]

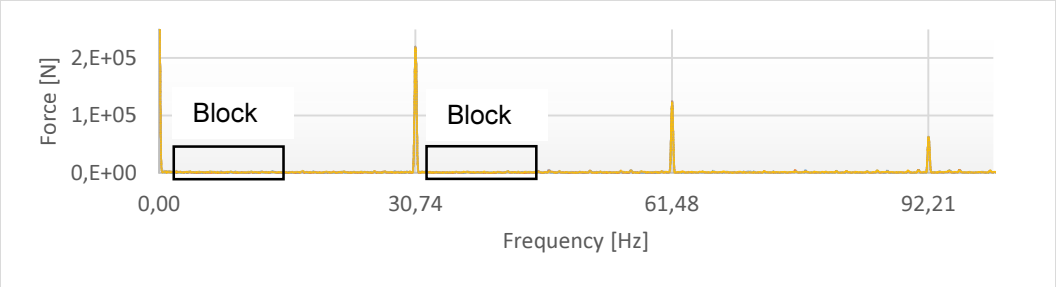

Figure 6-18: FFT of a cracked gear 1st stage

The 1st block (2 – 12Hz) is the frequency range right at the beginning of the curve. The first two Hz of the FFT are not considered due to high values at low frequencies of the FFT transformation. The observation range is 10 Hz. The 2nd block (32 – 42Hz) is defined right after the 1st GMF. To obtain values for the calculation that represents the system, the contact forces between the sun and all four planet gears have been considered for the calculation. Therefore the standard deviation of all four FFT´s have been averaged. These averaged values of the standard deviation have are compared to each crack length of the sun.

Due to the FFT transformation the magnitude of the curve is not representing the actual force and can just be considered to compare the results. That means that the value of the force in the FFT does not give information of the real force that has been applied. But the value can be used to compare other simulations to each other. This is only true if all parameters of the simulation have not been changed. The different crack sizes will lead to different forces in the FFT. These forces can be compared.

Therefore it is legitimate to compare the magnitude of the different results of the FFT analysis. Because the value of the FFT does not represent a real value, the units of the standard deviation will be neglected.

Table 6-4 shows the standard deviation of the FFT markers and operating numbers for a perfect gear. For the 1st Block the averaged standard deviation of all four planets is 555.83 and for the 2nd Block it is 508.01. These values are now the 100% base value that will be compared to the cracked gears in other simulations.

Table 6-4: Standard Deviation of the FFT markers and Operating Numbers for a Perfect Gear

		1st Block				2nd Block			
		Sun P1	Sun P2	Sun P3	Sun P4	Sun P1	Sun P2	Sun P3	Sun P4
Perfect Gear	**Standard Deviation**	532.37	466.58	687.07	537.32	528.3	535.06	409.20	559.5
	Standard Deviation Average	555.83				508.01			

Table 6-5 shows the standard deviation of the FFT markers and operating numbers for a middle cracked sun gear. For more information about the different cracks, see chapter 6.1 on page 62. The standard deviation is changing just by 2% in the 1st block and 0% in the 2nd. The small increase does not indicate a crack. Several simulations show that there are frequently small differences in the standard deviation even with perfect gears. Therefore the same simulation can have different results. Research has shown that the standard deviation has to change by a minimum of 20-40% to show a change in vibrational behavior due to changes of geometry or material condition

Table 6-5: Standard Deviation of the FFT markers and Operating Numbers for a Middle Crack

		1st Block				2nd Block			
		Sun P1	Sun P2	Sun P3	Sun P4	Sun P1	Sun P2	Sun P3	Sun P4
Middle Crack	**Standard Deviation**	481.32	681.75	605.15	552.68	358.05	568.93	579.11	532.22
	Standard Deviation Average	564.47				509.58			
	Standard Deviation Average, in % Difference	102 %				100 %			

Table 6-6 shows the standard deviation of the FFT markers and operating numbers for a long cracked sun gear. As shown, the long crack shows significant differences, more than 50%, in the average standard deviation. This shows that a crack can be detected with certainty. However, the long crack has already a significant length. That means that an installed damage detecting unit at the wind turbine gearbox can just detect cracks that will break soon.

Table 6-6: Standard Deviation of the FFT markers and Operating Numbers for a Long Crack

		1st Block				2nd Block			
		Sun P1	Sun P2	Sun P3	Sun P4	Sun P1	Sun P2	Sun P3	Sun P4
Long Crack	**Standard Deviation**	732.02	792.80	845.85	1000.90	875.94	696.32	918.50	1038.74
	Standard Deviation Average	842.89				882.37			
	Standard Deviation Average, in % Difference	152 %				174 %			

Table 6-7 shows the standard deviation of the FFT markers and operating numbers for an extra-long cracked sun gear. The averaged standard deviation difference is already 385% in the 1st Block and even more, 461%, in the 2nd Block.

Table 6-7: Standard Deviation of the FFT markers and Operating Numbers for an Extra Long Crack

		1st Block				2nd Block			
		Sun P1	Sun P2	Sun P3	Sun P4	Sun P1	Sun P2	Sun P3	Sun P4
Extra Long Crack	**Standard Deviation**	2168.8	2179.1	2062.5	2150.0	2379.1	2396.1	2265.5	2311.3
	Standard Deviation Average	2140.10				2342.88			
	Standard Deviation Average, in % Difference	385 %				461 %			

This shows that at the moment when the crack shows change in the vibrational behavior, the operating number is changing rapidly. This is a very good indicator that the system will have a tooth breakage soon. As discussed, the value of the standard deviation became higher as the crack in the tooth gets larger. **Figure 6-19** shows the increasing vibration noise occurs with a larger crack in the system.

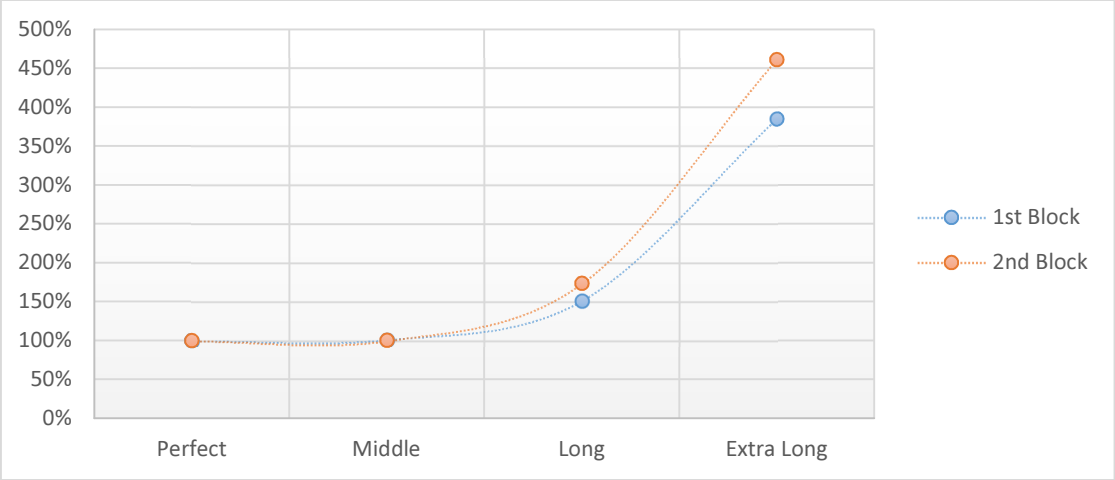

Figure 6-19: Increasing vibration noise with larger cracks

This is a very satisfying result. The simulation and analysis proves that vibration based planetary gear analysis and damage detection is possible for cracked teeth.

7 RECAP AND PERSPECTIVE

With this gained knowledge, it is possible to simulate flexible bodies with all different types of gear failures. With the comparison of vibrational behavior, which can be defined as an operating number, it is easy to determine damage in the wind turbine gear box. Additionally, the change of the operating number gives an indication of the dynamic progress of the damage. The next step is to apply the knowledge from the simulation on a real gearbox of a wind turbine. A control unit can be designed that measures the vibrational behaviors of the gear box with accelerometers. These measurements can be compared to the simulation results. If this is successful, all different kinds of vibrational behavior due to failure modes can be simulated. Another thesis project may consider analyzing the possibility to detecting a specific damages on a certain gear with the vibrational behavior of the gear box.

However, the simulation has shown that a vibration based planetary gear analysis and damage detection is possible for tooth root cracks.

REFERENCES

[1] "Pictures of wind turbines for media purpose," 18 March 2014. [Online]. Available: http://www.nordex-online.com/en/news-press/press-pictures.html.

[2] V. Quaschning, Regenerative Energiesysteme, Carl Hanser Verlag GmbH & Co. KG, 2013.

[3] Nordex N90/2300 Spec Sheet, 2003.

[4] R. Errichello, "Wind Turbine Gearbox Failures," GEARTECH, 2000.

[5] R. Errichello and J. Muller, "NREL: Gearbox Reliability Collaborative Gearbox 1 Failure Analysis Report," 2012.

[6] "Failure Modes," 25 March 2014. [Online]. Available: http://gearboxfailure.com/failure-modes-2/overload/plastic-deformation.

[7] DIN 3979 - Tooth damages on gears;, 1979.

[8] M. McDade, S. Sheng and R. Errichello, "NREL: Wind Turbine Gearbox Failure Modes – A Brief," ASME/STLE 2011 International Joint Tribology Conference, Los Angeles, California, 2011.

[9] H. Wittel, D. Muhs, D. Jannasch and J. Voßiek, Roloff/Matek Maschinenelemente, 21 ed., Springer Vieweg, 2013.

[10] E. v. d. Feen, IEC 61400-4 - Wind Turbines – Part 4: Design requirements for wind turbine gearboxes, International Electrotechnical Commission, IEC, 2009.

[11] MSC, MSC Adams Help 2013.2, 2013.

[12] K. L. Johnson, Contact mechanics, Cambridge: Press Syndicate of the University of Cambridge, 2004.

[13] I. Autodesk, "Engineer's Handbook," 9 September 2013. [Online]. Available: http://wikihelp.autodesk.com/Inventor/enu/2014/Help/1283-Inventor1283/4096-Engineer4096/4269-Transmis4269/4270-Spur_Gea4270/4271-Geometri4271/4279-Backlash4279.

[14] J. Dr.-Ing. Loomann, Zahnradgetriebe Grundlagen, Konstruktionen, Anwednungen in Fahrzeugen, Berlin Heidelberg: Springer-Verlag, 2009.

[15] T. Petrovic, I. Ivanov and M. Milosevic, "Anew structure of combined gear trains with high transmission ratios," *Forsch Ingenieurwesen,* no. DOI 10.1007/s10010-008-0085-9, p. 119–127, 2009.

[16] DIN 780 - Modulreihe für Zahnräder, DEUTSCHE NORMEN, 1977.

[17] DIN 867 - Bezugsprofile, DEUTSCHE NORM, 1986.

[18] 18 March 2014. [Online]. Available: http://www.connaissancedesenergies.org/qu-est-ce-que-le-petit-eolien.

[19] DIN 3967 - System of Gear Fits; Backlash, Tooth Thickness Allowances, Tooth Thickness Tolerances; Principles, Deutsche Norm, 1978.

[20] "Thyssen Krupp - Rothe Erde," 12 03 2014. [Online]. Available: http://www.thyssenkrupp-rotheerde.com/D/TG/Kopfflankenruecknahme.shtm.

[21] Nordex, "WINDPOWERUPDATE No. 26," Spring 2008.

[22] Dubbel - Taschenbuch für den Maschinenbau, Springer, 2011.

[23] K. Stahl, B.-R. Höhn and T. Tobie, "Tooth Flank Breakage – Influences on Subsurface Initiated Fatigue Failures of Case Hardened Gears," *ASME 2013 International Design Engineering Technical Conferences,* pp. DETC2013-12183, 2013.

[24] ISO 6336 - Calculation of Load Capacity of Spur and Helical Gears, 2006.

[25] A. Milburn, "Wind Turbine Gearbox Wear and Failure Modes and Detection Methods," 2011.

[26] H. Dinner, "Dem Wind die Zähne gezeigt," KISS soft.

[27] DIN 3990 T1, Deutsche Norm.

[28] U. E. I. A. U.S. Department of Energy, "International Energy Statistics, World," 2011.

[29] J. Giesbers, "CONTACT MECHANICS IN MSC ADAMS," University of Twenty, 2012.

[30] C. Verheul, "Contact Modeling".

[31] R. R. Craig and A. J. Kurdila, Fundamentals of Structural Dynamics, New Jersey: John Wiley & Sons, 2006.

[32] Özgüven and Houser, "Mathematical Models used in Gear Dynamics – A Review," *Journal of Sound and Vibration,* no. 121(3), pp. 383-411, 1988.

[33] Parey and Tandon, "Spur Gear Dynamic Models Including Defects: A Review," *The Shock and Vibration Digest,* vol. 35, no. 6, pp. 465-478, 2003.

[34] Parey, El Badaoui, Guillet and Tandon, "Dynamic modeling of spur gear pair and application of empirical mode decomposition-based statistical analysis for early detection of localized tooth defect," *Journal of Sound and Vibration,* vol. 294, p. 547–561, 2006.

[35] Lin and Parker, "Parametric Instability of Planetary Gears under Mesh Stiffness Variation," *Journal of Sound and Vibration,* vol. 249, pp. 129-145, 2002.

[36] Lin and Parker, "Analytical Characterization of the Unique Properties of Planetary Gear Free Vibration," *ASME Journal of Vibration and Acoustics,* vol. 121, pp. 316-321, 1999.

[37] Kong, Meagher, Xu, Wu and Wu, "Nonlinear Contact Analysis of Gear Teeth for Malfunction Diagnostics," *IMAC XXVI a Conference on Structural Dynamics, Society for Experimental Mechanics,* 2008.

[38] Sommer, Meagher and Wu, "Gear Defect Modeling of a Multiple-Stage Gear Train," *Modelling and Simulation in Engineering,* p. ID 754257, 2011.

[39] Wu, Meagher and Sommer, "A Differential Planetary Gear Model with Backlash and Teeth Damage," *IMAC XXIX a Conference and Exposition on Structural Dynamics, Society for Experimental Mechanics,* 2011.

[40] L. Papula, Mathematische Formelsammlung, Wiesbaden: Friedr. Vieweg & Sohn Verlag, 2006.

[41] "Cal Poly Formatting Guidelines," [Online]. Available: http://issuu.com/cont-ed/docs/master_s_thesis_and_project_formatt.

Guidance for gear design of wind turbines

Please note that the two following figures were originally one. They were spit due to space limitations and are connected via the three paths ending on the right and beginning on the left side respectively.

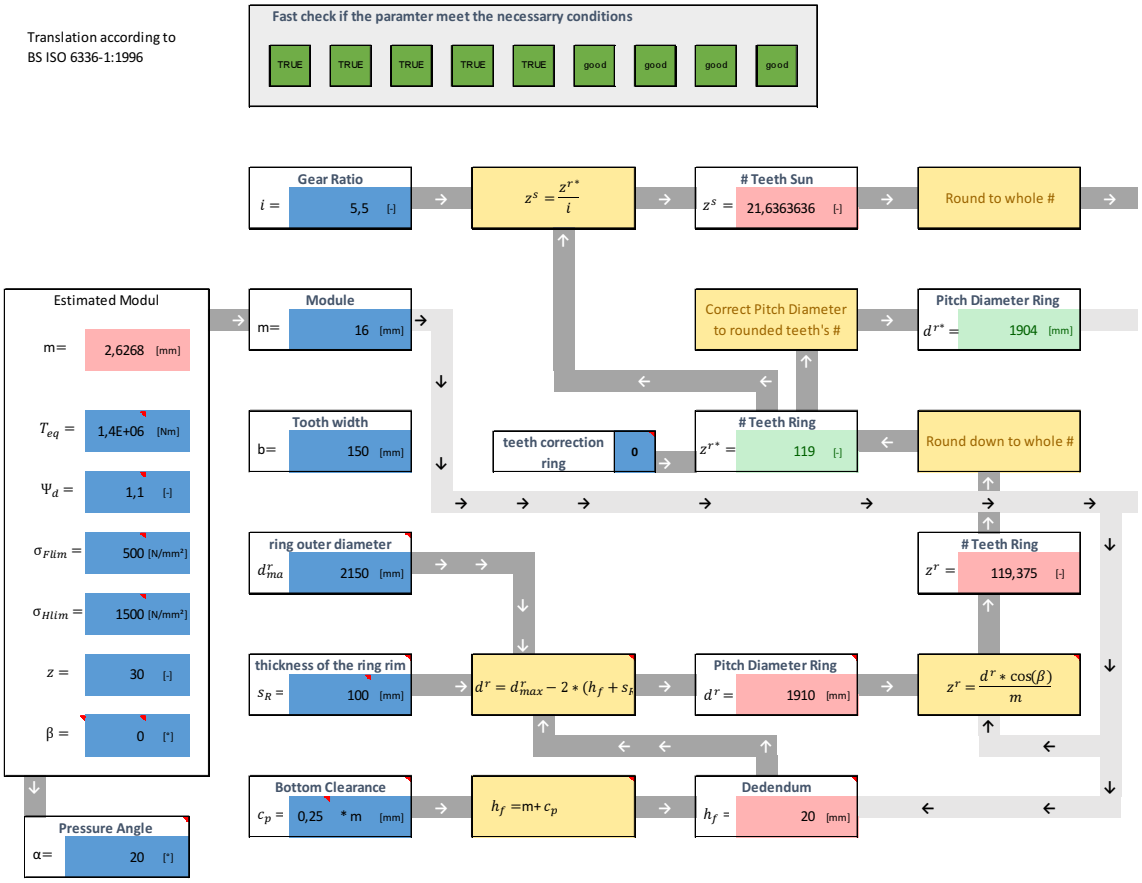

Figure: Guidance for gear design of wind turbines, part A

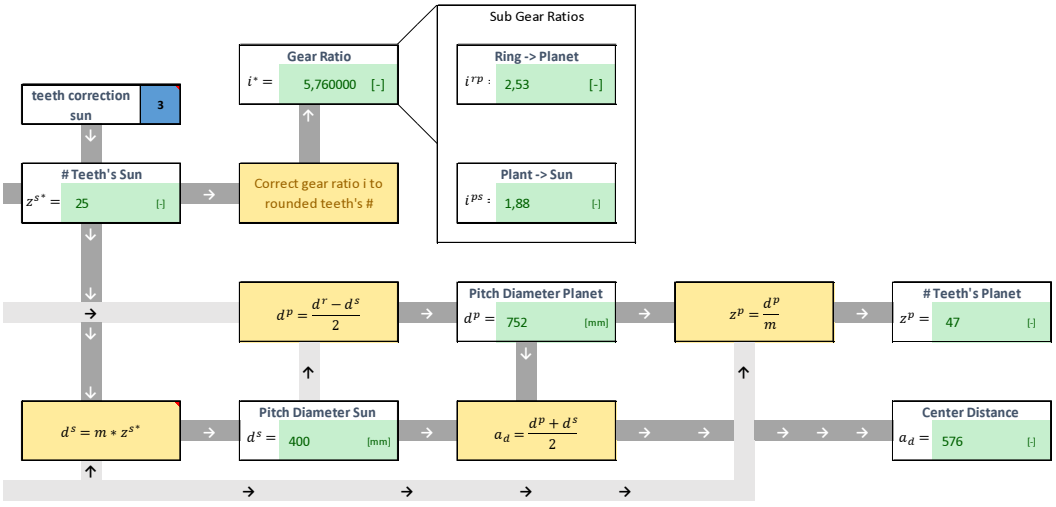

Figure: Guidance for gear design of wind turbines, part B

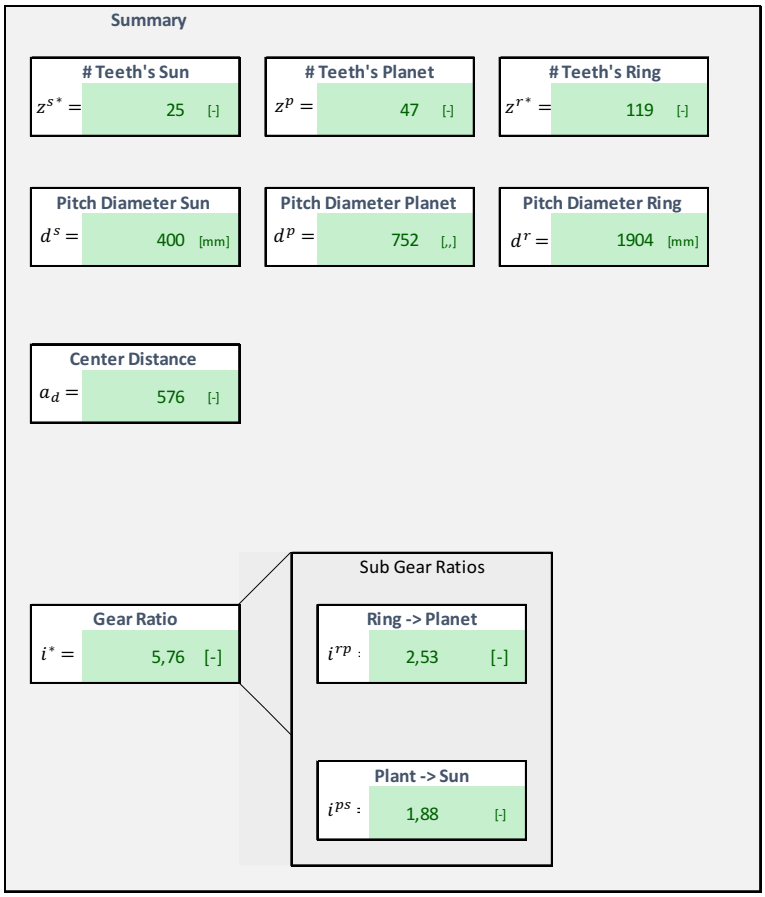

Figure: Summary of the results of the guidance calculations

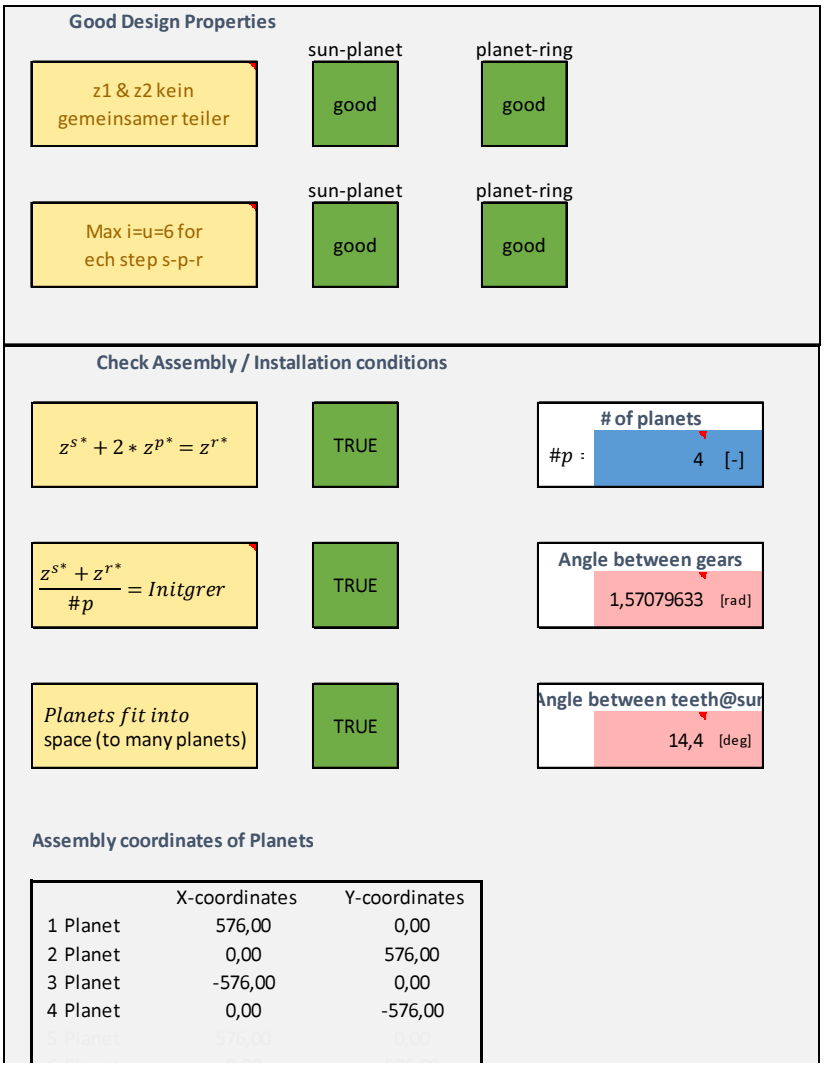

Figure: Results and assembly information of the guidance calculations

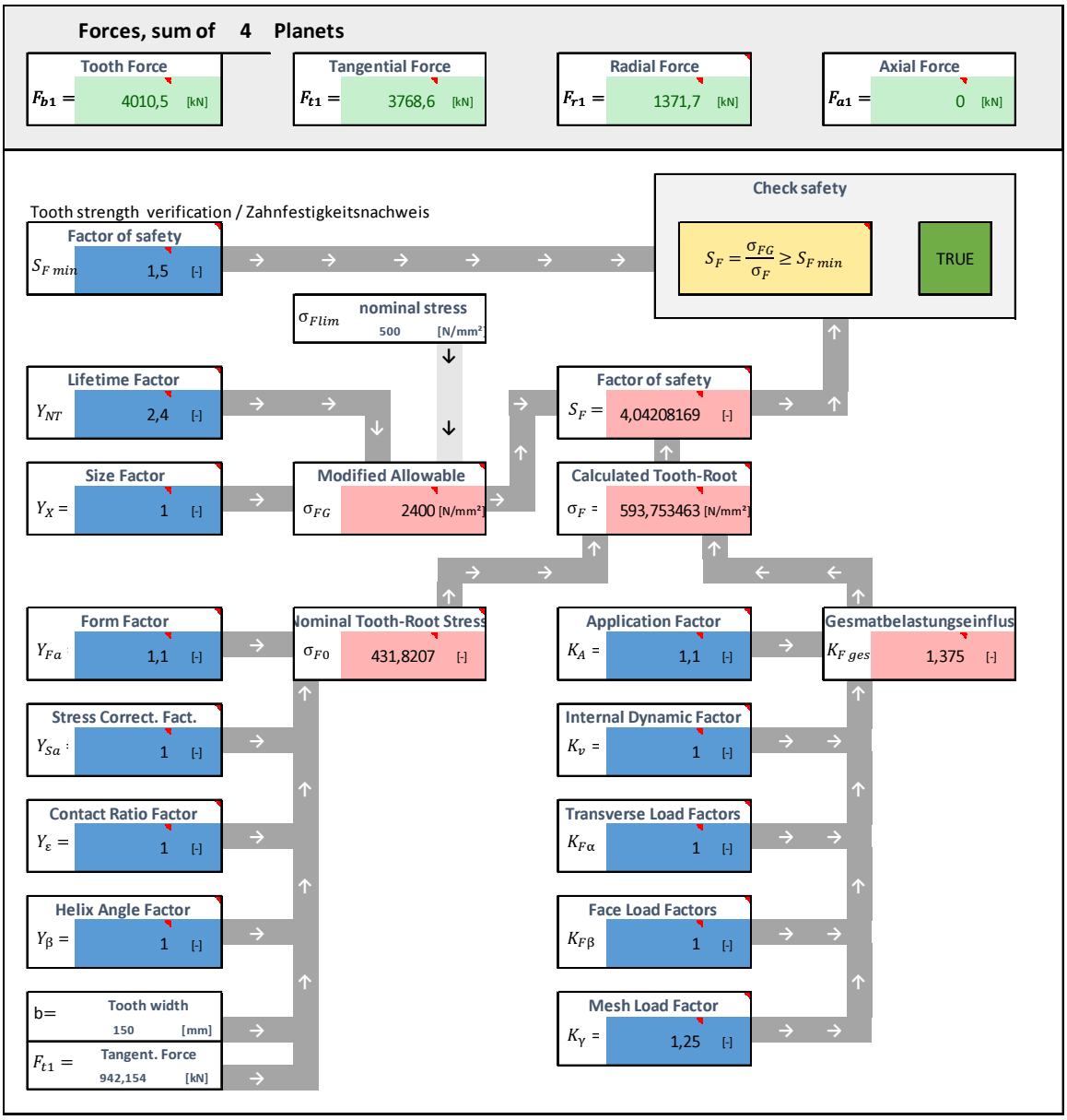

Figure: Tooth strength verification of the guidance calculations

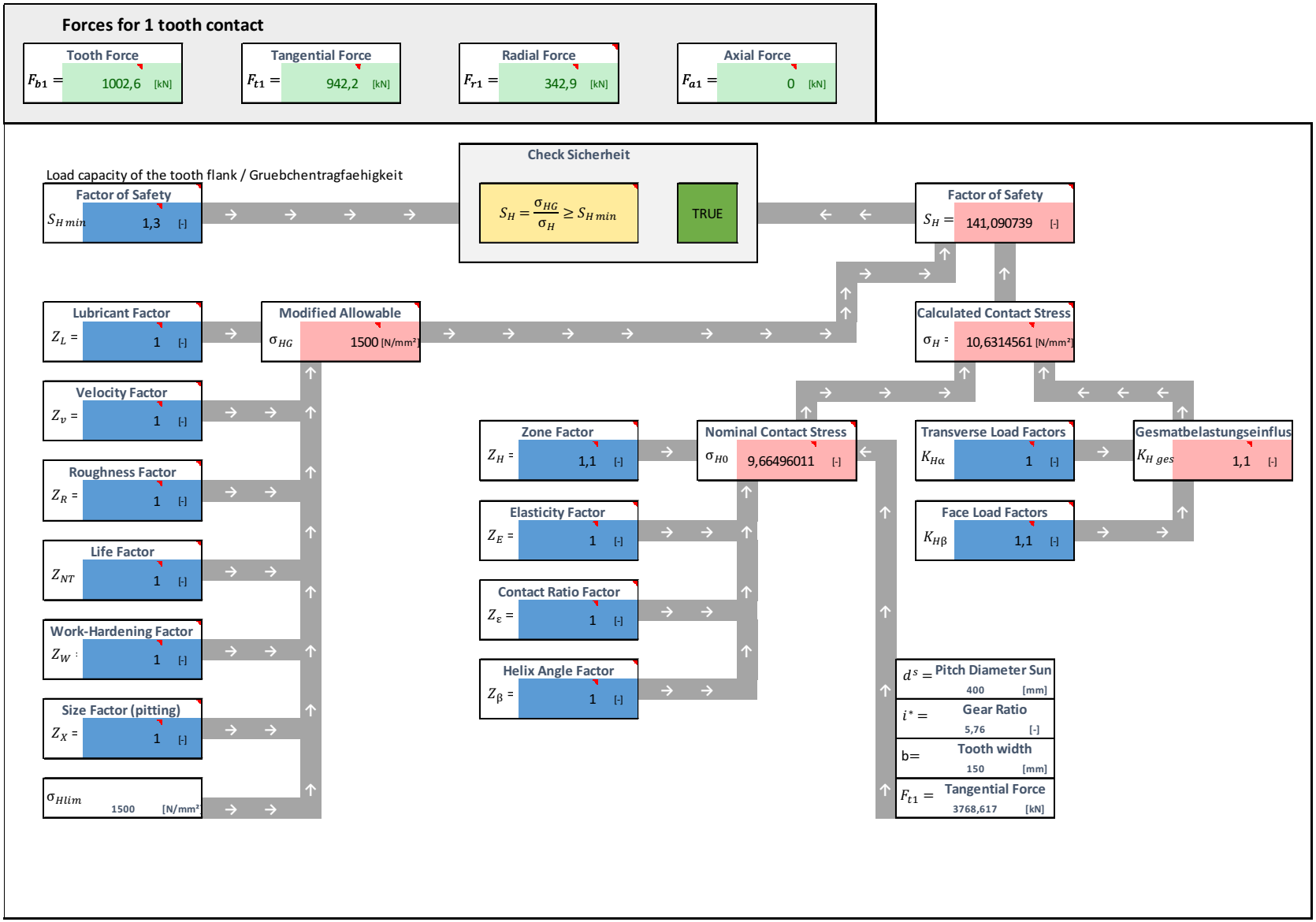

Figure: Load capacity of the tooth flank verification of the guidance calculations

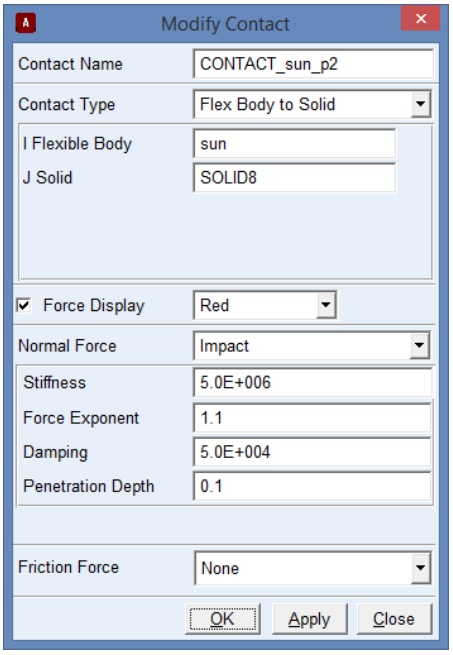

Figure: Contact parameters

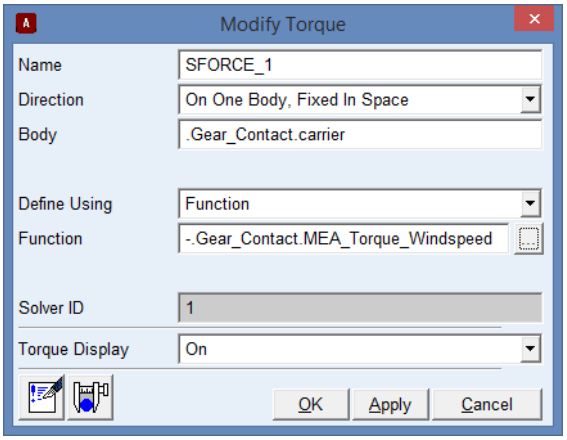

Figure: Applied torque on carrier

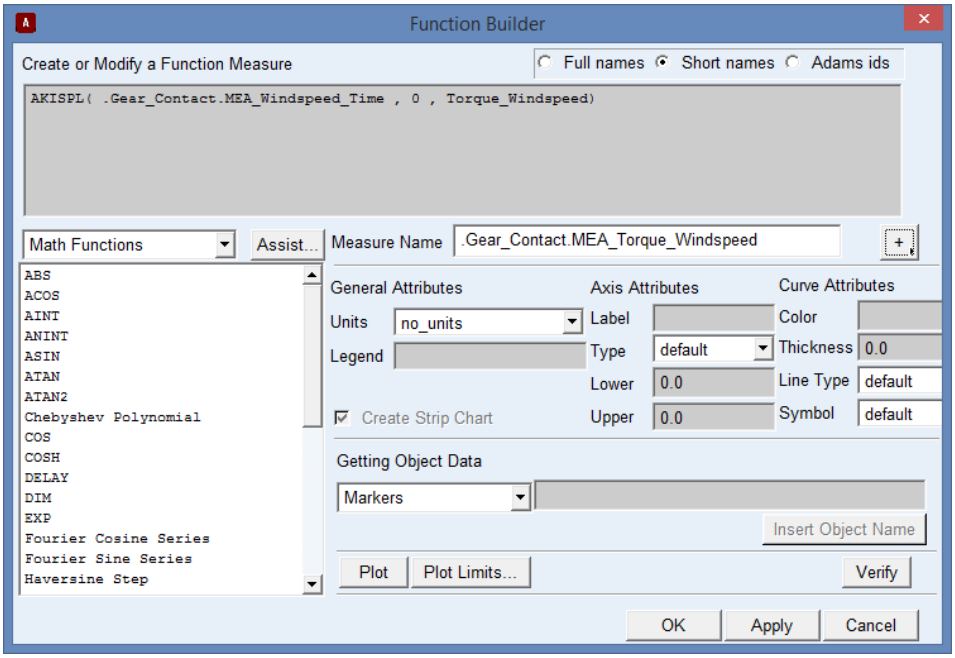

Figure: Torque function for the carrier based on wind speed and torque over wind speed

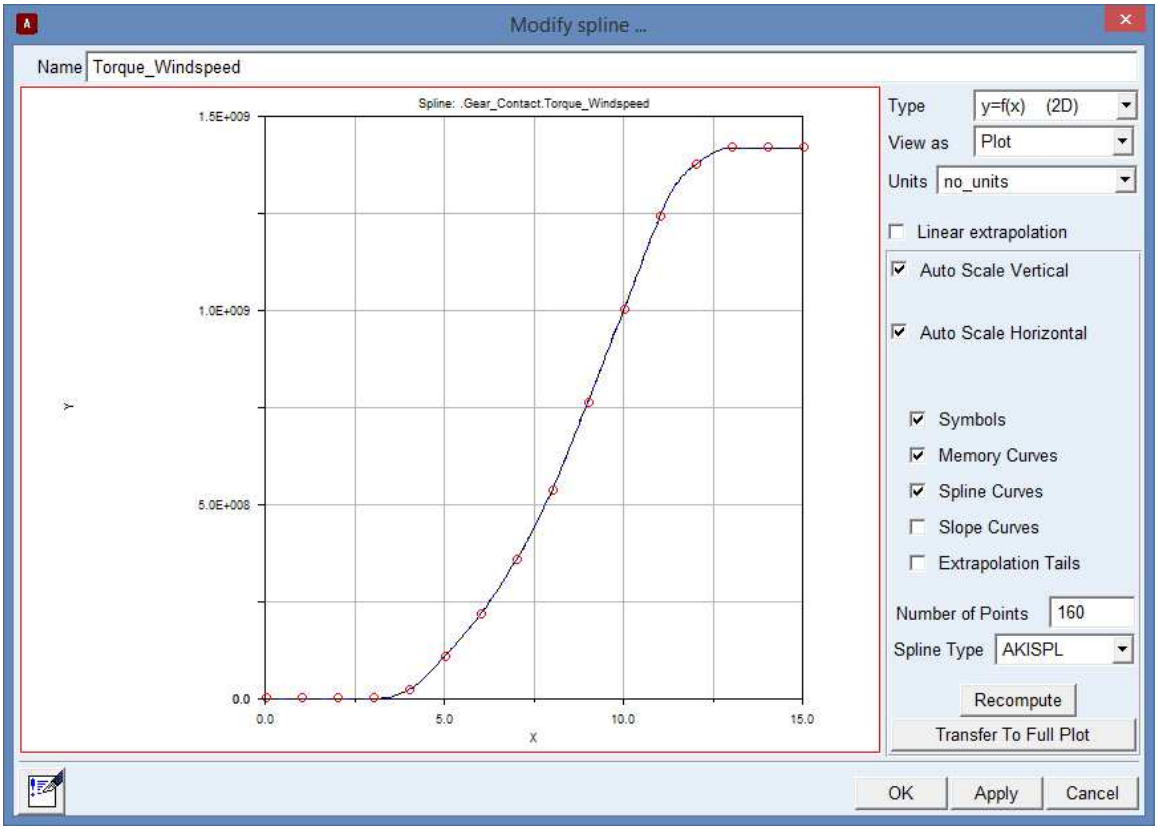

Figure: Torque over wind speed function based on N90/2300 technical specifications